Measuring surface-wave overtone phase velocities using a mode-branch stripping technique

Hendrik Jan van Heijst and John Woodhouse
Department of Earth Sciences, University of Oxford, Parks Road, Oxford, OX1 3PR, *UK. E-mail: hendrikv@earth.ox.ac.uk*

SUMMARY
We present a method for the retrieval of the phase velocities of surface-wave overtones. The 'single-station' method is successful for several Love and Rayleigh overtone branches (up to at least four) in mode-specific period ranges between 40 and 200 s. It uses mode-branch cross-correlation functions and relies on adjusting the phase and amplitude of the mode branches one at a time. A standard statistical optimization technique is used. We discuss in detail the *a priori* information that is added to stabilize the retrieval procedure. In addition, we present a technique to estimate the reliability of individual phase and amplitude measurements. The retrieval method and the technique to estimate reliabilities can be used together in a highly automated way, making the methods especially suited for studying the large volume of digital data now available.

We include several applications to synthetic and recorded waveforms. We will discuss in detail an experiment with 90 waveforms that have travelled along very similar paths from Vanuatu to California. For this path, we will present average overtone phase velocities and an average 1-D velocity structure.

Key words: seismic tomography, seismology, surface waves, waveform analysis.

1 INTRODUCTION

Since the early 1980s, global 3-D models of the mantle have been constructed using a variety of data and modelling techniques (e.g. Masters *et al.* 1982; Woodhouse & Dziewonski 1984, 1986, 1989; Dziewonski 1984; Giardini, Li & Woodhouse 1987; Tanimoto 1990; Su, Woodward & Dziewonski 1994; Woodhouse & Trampert 1997). As is the case in any modelling exercise, resolution is limited, but it improves as further data sets are incorporated. Naturally, it is desirable to achieve the greatest possible resolution, especially since there are important geodynamical questions which can only be addressed using more detailed models. At present, for example, global models are insufficiently well resolved to allow firm conclusions to be drawn concerning the scale lengths and correlation lengths associated with mantle convention in the transition zone, an issue of great significance in addressing the issue of 'whole-mantle' or 'layered-mantle' flow (Jordan *et al.* 1993).

A valuable potential source of information is provided by surface-wave overtone dispersion. Since overtones, at a given period, sample deep structure that is poorly sampled by the fundamental mode in retrievable frequency ranges, the incorporation of higher-mode dispersion data greatly improves the depth resolution (Der, Masse & Landisman 1970) and uniqueness (van Heijst, Snieder & Nowack 1994) of earth models. Overtones can also provide further information on the

shallow structure. Since a long-period body-wave seismogram can be thought of as a superposition of surface-wave overtones, information on overtone dispersion is already incorporated into global models using long-period body waveforms as part of the data (Woodhouse & Dziewonski 1984, 1986, 1989; Tanimoto 1990; Su *et al.* 1994). However, the modelling of waveforms has many inherent difficulties, and the detailed dispersion properties of overtones have not yet been measured.

In particular, in modelling waveforms, the strength with which a particular overtone enters into the inversion is governed solely by its excitation. Much more refined information could be extracted if it were possible to map the dispersion characteristics of the individual overtone branches. A further reason for wishing to measure overtone dispersion directly is that it would provide a much simpler constraint on mantle models than waveforms, which depend upon structure in a highly non-linear way. Also, there are difficulties in correctly calculating body waveforms in a 3-D earth model. The 'path integral approximation' (Woodhouse & Dziewonski 1984), which has been used in many studies, is known to be a relatively poor approximation for body-wave phases (Woodhouse 1983; Li & Tanimoto 1993) but probably remains a good approximation for the low overtone branches. This last issue has recently been addressed by incorporating mode coupling (Li & Romanowicz 1995) and, in a regional context, by Marquering & Snieder (1995).

Unfortunately, measuring higher-mode phase or group velocities is far from easy. Whereas the fundamental mode branch is often well separated from the other modes in the time domain, the higher modes interfere considerably. Overtones also overlap in the frequency domain, making the independent measurement of their properties difficult. Overtone branches can be separated in the (ω, k) domain using an array of seismometers, as was first shown by Nolet (1975, 1977) and later applied by several others (e.g. Mitchell 1980; Okal & Jo 1987; Cara 1978). Using array techniques, it is possible to measure the average fundamental- and higher-mode phase velocities under the array, which can be inverted for structure in a straightforward way. Clearly, the use of this method is restricted to areas where dense arrays of seismographs are available, and cannot be used in global modelling.

Overtone information has been included in global models using full waveform inversion techniques. Full waveform methods aim to fit synthetic waveforms to recorded waveforms, including the overtones, to constrain the average structure between a source and a receiver. In the alternative approach of Lerner Lam & Jordan (1983, 1987), which was adopted and extended by Cara & Leveque (1987), path-averaged structure is not directly constrained by the full waveform. Instead, a path-averaged structure is determined from branch cross-correlation functions (bccfs) for several mode branches. In essence, the cross-correlations with synthetic mode branches are used to increase the sensitivity to the overtone information.

Recently, powerful highly automated procedures to retrieve fundamental-mode phase velocities have made it possible to construct high-resolution global fundamental-mode phase-velocity maps in a wide frequency band (Trampert & Woodhouse 1995). Inverting phase-velocity maps for upper-mantle structure is straightforward, and fundamental-mode maps have proved to be powerful constraints on the structure of the top of the upper mantle. The automated methods rely on making very large numbers of independent phase measurements (some 60 000 in Trampert & Woodhouse 1996) that are not constrained by path-averaged structures. As the measurements are not constrained to correspond to path-averaged structures, they can be interpreted not only in terms of local phase-velocity perturbations, but potentially also in terms of, for instance, ray bending, physical dispersion, source characteristics and anisotropy. Ideally, we would like to be able to make similar measurements for surface-wave overtones.

So far, only one method has been proposed to measure path-averaged dispersion of surface-wave overtones (Stutzmann & Montagner 1993, 1994). In this method, several sources at different depths in a small area are used to constrain overtone phase-velocity perturbations. The requirement of several sources at different depths greatly reduces the number of available paths. This leads to poor lateral resolution of the phase-velocity maps and the derived 3-D earth models.

In this paper, we introduce a new mode-branch stripping method that uses Lerner Lam & Jordan's bccfs. The method enables us to measure path-averaged phase velocities and amplitude perturbations for the fundamental mode and several overtones independently. An essential element of our technique is that we are able to assess the quality of the measurements in a quantitative way, which enables us to reject or to weight each measurement accordingly. This makes a high degree of automation possible and allows convenient study of the large volume of digital data now available. As will be shown in a subsequent contribution, this method can be used to construct high-resolution overtone phase-velocity maps.

2 PRELIMINARIES

A seismogram in a spherical reference model, in our case PREM (Dziewonski & Anderson 1981), corrected for ellipticity and rotation, can be represented as follows:

$$S_0(t) \approx \sum_k A_k \exp(i\omega_k t), \tag{1}$$

where the sum is over all multiplets k, A_k representing the source- and receiver-dependent amplitudes and ω_k the complex eigenfrequency of a multiplet.

We approximate a seismogram $S(t)$ in the heterogeneous earth as follows:

$$S(t) \approx \sum_k a_k A_k \exp[i(\omega_k + \delta\omega_k)t], \tag{2}$$

where a_k and $\delta\omega_k$ are real quantities, a_k accounting for amplitude and $\delta\omega_k$ for phase perturbations of each multiplet.

Usually the multiplets are thought of in terms of mode branches. The mode branch number n is defined as the overtone number at a fixed angular order. We write:

$$S(t) \approx \sum_q \sum_n \sum_l a_{ql}^n A_{ql}^n \exp[i(\omega_{ql}^n + \delta\omega_{ql}^n)t], \tag{3}$$

where n is the overtone number, starting at 0 for the fundamental mode, and l is the angular order. Index q stands for toroidal or spheroidal. Henceforth, we omit the index q and assume either toroidals or spheroidals. To facilitate their measurement, we approximate a_n^l and $\delta\omega_l^n$ as smooth functions of l, and therefore also ω, expanded in cubic splines, such that

$$\delta\omega_l^n = \delta\omega^n(\omega_l^n) \quad \text{and} \quad \delta\omega^n(\omega) = \sum_{i=1,M} x_i^n D_i(\omega), \tag{4}$$

$$a_l^n = a^n(\omega_l^n) \quad \text{and} \quad a^n(\omega) = \sum_{i=1,M} y_i^n D_i(\omega), \tag{5}$$

where $D_i(\omega)$ are the cardinal or base functions for cubic spline interpolation (e.g. Nonweiler 1984) corresponding to the nodes of the parametrization, $\bar{\omega}_i$. M is the number of nodes and basis functions and x_i^n and y_i^n are the coefficients we seek to retrieve from a seismogram.

The physical justification for assuming smoothly varying phase and amplitude perturbations is that within the same surface-wave overtone branch, multiplets of neighbouring angular order have only slightly different depth-dependent eigenfunctions and therefore have similar sensitivities to heterogeneous structure. For spheroidal modes, the surface-wave overtone branches are intersected by Stonely wave and core-mode branches. We omit these branches from the overtone numbering scheme, so that constant n corresponds to a smooth overtone branch in which neighbouring modes have similar physical characteristics (e.g. Okal 1978). We thus represent the relevant part of the seismogram as follows:

$$S(t) \approx \sum_n \sum_l a_l^n A_l^n \exp[i(\omega_l^n + \delta\omega_l^n)t]. \tag{6}$$

The expectation that a surface-wave seismogram in a 3-D model can be described in terms of smoothly varying

amplitude and phase functions is a consequence of surface-wave ray theory (see e.g. Woodhouse 1974; Tromp & Dahlen 1992a,b). Although such theories are valid only for the case in which the scale lengths associated with heterogeneity are large compared to the wavelength of the surface wave, the spectrum of heterogeneity in the Earth seems to be such that surface-wave ray theory remains a good approximation even for long-period surface waves, to which it has been extensively applied (see Zhang & Lay 1996 and references therein). Here, we assume surface-wave ray theory to be applicable for the surface-wave overtones as well as for the fundamental mode.

The *mode branch seismogram*, $u_n(t)$, will be defined as the contribution to (6) corresponding to a particular spheroidal or toroidal branch. We have

$$u_n(t) = u_n(t, x^n, y^n) = \sum_l a^n(\omega_l^n) A_l^n \exp\left[i(\omega_l^n + \delta\omega^n(\omega_l^n))t\right], \quad (7)$$

and the complete seismogram can be represented as a sum over overtone branches:

$$S(t) = \sum_n u_n(t). \quad (8)$$

Finally, we introduce a *reduced seismogram* $S^{-pq\cdots}(t)$:

$$S^{-pq\cdots}(t) = \sum_{n \neq p, n \neq q, n \neq \cdots} u_n(t), \quad (9)$$

which is simply the sum of all branches except $pq \ldots$. In the following, we shall write $S(t)$ for the data seismogram, thought of as being a superposition of branch seismograms $u_n(t)$, given by (4), (5), (6) and (7) and corresponding to certain x^n and y^n. We pose the problem of estimating x^n and y^n from the data. The corresponding estimated values will be denoted by $\tilde{x}^n$ and $\tilde{y}^n$ and the corresponding theoretical seismograms by $\tilde{u}_n(t)$, $\tilde{x}^n$, etc.

All the above definitions apply to synthetics as well. Note that in the rest of this paper, synthetic seismograms and corresponding coefficients such as x^n and y^n will be denoted with a tilde, that is $\tilde{u}_n(t)$ and $\tilde{x}^n$.

3 GENERAL OUTLINE OF THE RETRIEVAL ALGORITHM

In this section we give a general outline of how we retrieve the phase and amplitude perturbation coefficients x_i^n and y_i^n, defined above, from a seismogram. We will illustrate the essential steps of the technique with an application to a real-data seismogram.

The objective function that we minimize as a function of the amplitude and phase coefficients is a normalized version of Lerner-Lam & Jordan's bccf $O_n(\tau)$:

$$O_n(\tau) = S(t) * \tilde{u}_n(t) - \tilde{S}(t) * \tilde{u}_n(t), \quad (10)$$

or, writing the dependences on phase and amplitude perturbations explicitly,

$$O_n(\tau) = O_n(\tau, \tilde{x}^0 \ldots \tilde{x}^{n\max}, \tilde{y}^0 \ldots \tilde{y}^{n\max})$$

$$= (S(t) - \tilde{S}(t, \tilde{x}^0 \ldots \tilde{x}^{n\max}, \tilde{y}^0 \ldots \tilde{y}^{n\max})) * \tilde{u}^n(t, \tilde{x}^n, \tilde{y}^n),$$

$$(11)$$

where $S(t)$ represents a real seismogram, $\tilde{u}^n(t, \tilde{x}^n, \tilde{y}^n)$ a synthetic mode-branch seismogram as defined in eq. (7) and $\tilde{S}$

the full synthetic seismogram. The asterisk denotes cross-correlation and $n\max$ is the highest overtone number considered in the synthetics. The cross-correlation is used to enhance the signal-to-noise ratio and the dependence of $O_n(\tau)$ for small lag times on the difference between the assumed dispersion for mode branch n and the actual dispersion as present in the data (Lerner Lam & Jordan 1983). In the method of Lerner Lam & Jordan (1983), bccfs for several mode branches are used together in one inversion to constrain the average structure along the path between source and receiver. Here, on the other hand, we consider only one bccf at a time, in order to measure the coefficients $\tilde{x}^n$ and $\tilde{y}^n$ for each branch independently.

For these purposes, we would like $O_n(\tau)$ to be solely dependent on the differences between the phase and amplitude coefficients of branch n in the synthetic and the data. However, eq. (11) is clearly dependent on many more coefficients than just the amplitude and phase perturbations for mode n. Rewriting eq. (11) in terms of reduced seismograms, and suppressing dependence on the amplitude and phase coefficients, we may write:

$$O_n(\tau) = (u_n(t) - \tilde{u}_n(t)) * \tilde{u}_n(t) + (S^{-n}(t) - \tilde{S}^{-n}(t)) * \tilde{u}_n(t), \quad (12)$$

where $u_n(t)$ denotes the 'true' component of $S(t)$ corresponding to branch n. Expression (12) has two contributing terms: the first represents a function that is solely dependent on mode branch n, whereas the second describes the interference of branch n with all other branches. Ideally we would like the objective function to be independent of branches other than n, which corresponds to the second term being zero. There are three distinct cases where the influence of the second term is negligible:

(1) branch n happens to be dominant in the seismogram, $u_n(t) \gg S^{-n}(t)$;

(2) the reduced synthetic and real seismograms are almost equal, $S^{-n}(t) - \tilde{S}^{-n}(t) \approx 0$;

(3) for small lag times, if the interference in the time domain between $S^{-n}(t)$ and $\tilde{S}^{-n}(t)$ and $\tilde{u}_n(t)$ is small.

From these three conditions it is evident why resolving the phase and amplitude perturbation of the fundamental mode will generally be possible, as in most seismograms conditions (1) and (3) are both satisfied for the fundamental mode, especially for shallow sources (strong excitation of the fundamental) and long paths (little interference). For overtones, the situation is usually more difficult, as none of the above conditions is automatically satisfied. In our method, we seek to satisfy conditions (1) and (2) as well as possible by fitting branches in order of decreasing power, as will be explained below. Furthermore, we use a frequency-stepping procedure, solving and extrapolating from low frequencies to progressively higher frequencies. Thus, the difference between assumed and true dispersion will be small for most frequency steps, rendering the inverse problem more linear and the term $S^{-n}(t) - \tilde{S}^{-n}(t)$ small. Moreover, the frequency stepping usually prevents the phase-perturbation curve from locking into the wrong 2π cycle.

Schematically, our algorithm consists of the following steps.

(1) To avoid 2π phase jumps, we do not seek to solve the phase perturbations of a mode branch in a wide frequency range at once, but instead we start to solve for $\delta\omega^n$ at low

frequencies, where 2π phase-shifts from the reference model are not to be expected. Then, using the inherent smoothness of the branches, we trace the phase perturbation to higher frequencies step by step. We effectively do this by shifting a frequency window from lower to higher frequencies, minimizing eq. (10) within each window and extrapolating the results to higher frequencies. This step ensures locking of the branch into the correct 2π cycle, provided we can trace it from sufficiently low frequencies.

(2) Within each frequency window, we seek to minimize eq. (10) for as many overtones as possible. We start with the strongest branch and solve for other branches in order of decreasing power. The power of each branch is estimated from synthetics. This generally ensures that the larger part of $O_n(\tau)$ can be attributed to the mode branch n being retrieved, provided the stronger branches have been adequately fitted.

(3) The retrieval procedure for the most powerful branch, p, is carried out only if the maximum amplitude of the synthetic mode-branch seismogram exceeds the average amplitude of the data seismogram $S(t)$ by a pre-set threshold value. If this threshold is not met, the frequency window is moved to higher frequencies, where step (2) and this step are repeated. This condition avoids attempts to fit data that are too noisy.

(4) If condition (3) is met, $O_p(\tau)$ is calculated and minimized for phase in the time domain using a statistical inversion technique.

(5) If step (4) converges, the amplitude perturbations are determined. This is a straightforward linear problem, as the phase has already been fitted.

(6) If the minimization of phase and amplitude has been accomplished for the most powerful mode branch, p, we subtract the synthetic mode-branch seismogram $\tilde{u}_p(t)$ from the data $S(t)$ and omit it from the 'full' synthetic $\tilde{S}(t)$ in eq. (10). This renders the reduced synthetic seismogram $S^{-p}(t)$ and an approximate reduced data seismogram $\tilde{S}^{-p}(t)$.

(7) Next, the maximum amplitude of the next strongest mode branch, q, is compared as in (3) to the average amplitude of the reduced data seismogram, $S^{-p}(t)$. If the branch is strong enough compared to the reduced seismogram, it is likely that the previously considered branch has been fitted correctly and that the remaining reduced seismogram is clean enough to measure the phase and amplitude of this next most powerful branch.

(8) If condition (7) is met, a new objective function, $O_q(\tau)$, is calculated for branch q using the reduced seismograms. Omitting the obvious dependence on other branches, we write:

$$O_q(\tau) = O_q(\tau, \tilde{x}^q, \tilde{y}^q)$$
$$= S^{-p}(t) * \tilde{u}^q(t, \tilde{x}^q, \tilde{y}^q) - \tilde{S}^{-p}(t) * \tilde{u}^q(t, \tilde{x}^q, \tilde{y}^q), \qquad (13)$$

which should be predominantly dependent on the amplitude and phase perturbations of branch q.

(9) Now, $O_q(\tau)$ is minimized for the phase and amplitude of branch q, following the same steps (4) and (5). After convergence, the resulting mode branch seismogram is subtracted from $S^{-p}(t)$ to give $S^{-pq}(t)$ and omitted from $\tilde{S}^{-p}(t)$ to give $\tilde{S}^{-pq}(t)$. The whole process is repeated for the most powerful branch remaining, unless condition (7) can no longer be satisfied.

(10) If the threshold value in (7) is not reached, the minimization attempts within the current frequency window are abandoned. We then use the intrinsic smoothness of the phase

and amplitude perturbations to extrapolate the values of $\tilde{a}^n(\omega)$ and $\delta\tilde{\omega}^n(\omega)$ to higher frequencies. After this, the frequency window is shifted up to higher frequencies and the whole process (2) to (10) is repeated.

For both amplitudes and phase, the minimization of eq. (10) is carried out within a frequency-dependent lag-time window. This accounts for the fact that the cross-correlation at low frequencies gives rise to a broader signal in the lag-time domain than at high frequencies. The technique, as formulated, does not allow for the mode-branch seismograms to contain more than a single group arrival (e.g. $R1$ or $R2$). Windowing in the time domain is carried out in order to minimize contamination from other wave groups.

3.1 An example

The basics steps of the algorithm are most easily understood from an example. In Fig. 1(a) we show a vertical-component data trace together with the corresponding synthetic calculated for PREM. The event, $M6.2$ at 390 km depth in the Fiji region (event 071192A in the Harvard CMT catalogue), was registered at station HRV (Harvard). To calculate the synthetics, we use Harvard CMT solutions, which have proven to be sufficiently reliable in fundamental-mode studies (Trampert & Woodhouse 1995). We have convolved the synthetics with the instrument response to allow a comparison of data and synthetics. A low-pass filter with a cut-off period of approximately 60 s used.

In Fig. 1(b) we show the data together with the synthetics after adjusting the phase and amplitude of the lowest eight Rayleigh branches in specific frequency ranges using the mode-branch stripping technique. The agreement between data and synthetics is clearly very good, which means that we have found a combination of amplitude and phase perturbations for several mode branches that explains the data very well. Whether this is the correct and unique solution is an essential question, which is very difficult to answer. We will address this question using tests on synthetics and data in Sections 6.1, 6.2 and 7.

In Fig. 2 we show some of the steps that lead to the final waveform fit. The most important steps, cross-correlation $\Rightarrow$ inversion $\Rightarrow$ subtraction, are shown for three different mode branches in one frequency window. In this specific window, all traces are bandpass filtered around approximately 110 s. Traces are arranged in groups of three seismograms, (data, full synthetic and mode-branch synthetic) at the right and two corresponding cross-correlations (data * branch synthetic and synthetic * branch synthetic, where * denotes cross-correlation) at the left. All traces are scaled with respect to their maximum amplitude.

The very top trace in the figure is the real data $S(t)$ and the second trace is $\tilde{S}(t)$. The third trace is the mode-branch seismogram for the strongest branch in this window, the fundamental mode, $\tilde{u}_0(t)$. Both synthetic traces are the traces before inversion, but after extrapolation of the phase and amplitude from lower frequencies. The two cross-correlations to the left of the arrow 'cross-correlation' are $S(t) * \tilde{u}_0(t)$ and below it $\tilde{S}(t) * \tilde{u}_0(t)$. In the inversion process (steps 4 and 5 in the previous section) the difference between these two cross-correlations is minimized. The cross-correlations after inversion are shown below the arrow 'inversion'. The data and the resulting full synthetic and mode-branch seismograms are
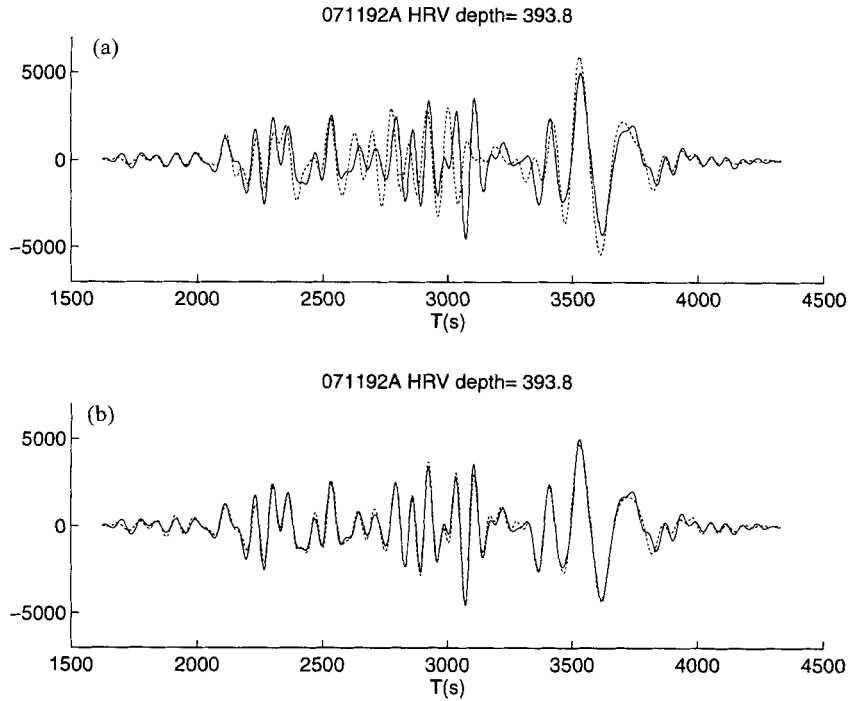
071192A HRV depth= 393.8

071192A HRV depth= 393.8

Figure 1. (a) Recording (solid line) at station HRV of surface waves excited by an event in the Fiji region. The corresponding synthetic waveform (dotted line) is calculated for PREM using the Harvard CMT source mechanism. The waveforms are both low-pass filtered, cut-off at $T = 60$ s. (b) Same data trace (solid line). The synthetic (dotted line) is obtained after adjusting the phase and amplitude for several mode branches.

plotted to the right of the arrow 'result', in the same order as above. The next step after inversion is subtraction: $\tilde{u}_0(t)$ is subtracted from the data and omitted from the synthetic to give (an approximation to) $S^{-0}(t)$ and $\tilde{S}^{-0}(t)$, which are the two first traces below the arrow 'subtraction'. These two reduced seismograms are cross-correlated (steps 7 and 8) with the next most powerful branch, $\tilde{u}_1(t)$, plotted below the two reduced seismograms. For this branch the inversion and subtraction are repeated to give $S^{-01}(t)$ and $\tilde{S}^{-01}(t)$. Finally, the phase and amplitude of the next, second overtone branch are optimized, as shown in the bottom 10 traces. As the fourth most powerful branch did not pass the condition of step (7) in the previous section, the procedure was terminated in this frequency window.

In this example, the frequency stepping works well. The phases of the fundamental mode and the first overtone are already well matched before inversion, because for both these branches, the phase and amplitude have been extrapolated from lower frequencies. However, for the second overtone, this is the first window that the branch is solved for and clearly the phase difference before inversion is much larger for this branch than for the other two.

The reduced data traces look very clean after subtraction of the fundamental mode and first overtone and are very similar to the synthetic reduced seismograms. Moreover, the bccfs for all three branches are very clean, suggesting that the objective functions are predominantly dependent on the target mode branch. Finally, note from the top trace how weak the second overtone signal is compared to the fundamental mode and how much the branch stripping enhances the dependence of the objective function for this mode branch.

The procedure outlined above generally ensures the locking of phase in the correct cycle. Moreover, it reduces the,

normally very strong, non-linearity of the inversion at higher frequencies, as the frequency stepping and extrapolation result in good initial estimates of the phase perturbations.

4 DETAILED DESCRIPTION OF THE RETRIEVAL ALGORITHM

In this section, we describe several aspects of the retrieval algorithm in more detail: frequency stepping, resolving phase perturbations, resolving amplitudes, the parametrization, the *a priori* information that is added and smoothness constraints.

4.1 Frequency stepping and extrapolation

An essential part of the inversion algorithm is the 'frequency stepping', as mentioned under (1) in Section 3.1. The window that is moved through the frequency domain is defined in terms of the nodes of the parametrization $\bar{\omega}_i$, the window length w and two cosine tapers. The phase and amplitude perturbations of all branches are parametrized using the same nodes $\bar{\omega}_i$. Denoting a window with a lower frequency limit $\bar{\omega}_l$ by $W_l(\omega)$, we write:

$$W_l(\omega) = \begin{cases} 0 & \omega \leq \bar{\omega}_l \\ \frac{1}{2}\left(1 - \cos\pi\frac{\omega - \bar{\omega}_l}{\bar{\omega}_{l+1} - \bar{\omega}_l}\right) & \bar{\omega}_l \leq \omega \leq \bar{\omega}_{l+1} \\ 1 & \bar{\omega}_{l+1} \leq \omega \leq \bar{\omega}_{l+w-1} \\ \frac{1}{2}\left(1 + \cos\pi\frac{\omega - \bar{\omega}_{l+w-1}}{\bar{\omega}_{l+w} - \bar{\omega}_{l+w-1}}\right) & \bar{\omega}_{l+w-1} \leq \omega \leq \bar{\omega}_{l+w} \\ 0 & \omega \geq \bar{\omega}_{l+w} \end{cases}$$
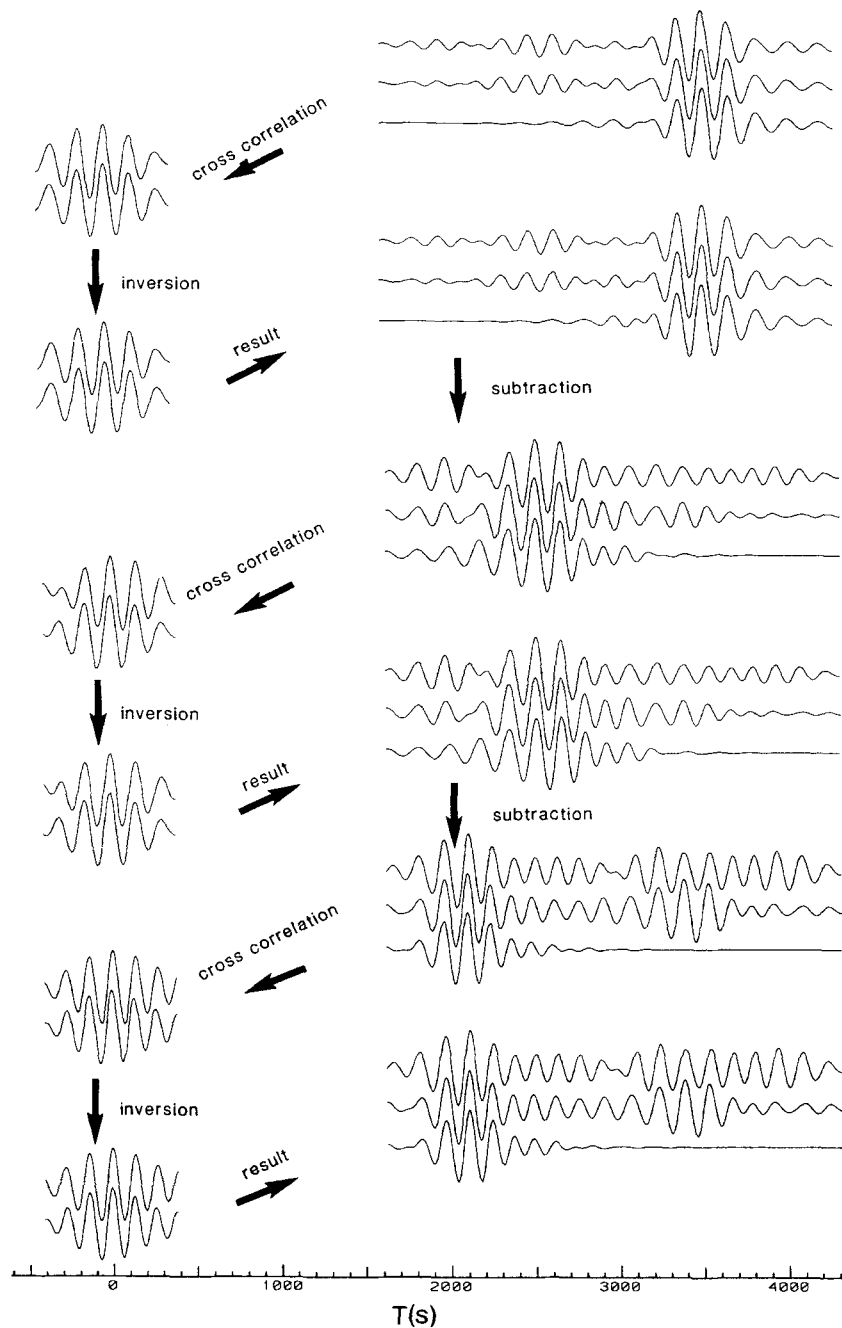
(14)

Figure 2. Schematic illustration of the most important steps of the retrieval algorithm. See text for details.

The 'next' frequency window in the stepping procedure is simply given by $W_{l+1}(\omega)$, which is the whole window shifted up one node in the frequency domain. By moving the window up only one node for each step, the perturbations at most nodes will be considered several times in overlapping frequency windows, allowing a rough determination of the perturbation in the first step and refinement of the measurement in subsequent steps. Having found phase-velocity and amplitude perturbations, the results are extrapolated to higher frequencies. Extrapolating from window $W_l(\omega)$ to the next window $W_{l+1}(\omega)$, the phase and amplitude perturbations at all higher-frequency nodes are set to be equal to the perturbations at the highest-frequency node that has already been

solved for. For the phase-velocity perturbations, this becomes, explicitly,

$$\tilde{x}^n_i = \tilde{x}^n_{l+w} \quad l+w+1 \le i \le M , \tag{15}$$

where M is the number of nodes used in the parametrization.

4.2 Retrieval of phase-velocity perturbations

Within each of the frequency windows defined above, we use a standard statistical optimization technique (Tarantola & Valette 1982a,b) to retrieve the phase perturbations. In this section, we will refer to the perturbations for a given mode branch, $\tilde{x}^n$, as the 'model'. We define the theoretical

relationship between data and model as a normalized version of the bccf eq. (10). Omitting the dependence on $\tilde{y}^n$ and branches other than n, we write:

$$g(\tau, \tilde{x}^n) = \frac{S'(t) * \tilde{u}_n(t, \tilde{x}^n) - \tilde{S}'(t, \tilde{x}^n) * \tilde{u}_n(t, \tilde{x}^n)}{\|S'(t) * \tilde{u}_n(t, \tilde{x}^n)\|}, \tag{16}$$

where the primes in $S'(t)$ and $\tilde{S}'(t)$ stand for either full seismograms or reduced seismograms, which are treated in exactly the same way, as discussed in Sections 3 and 3.1. In the lowest-frequency window that perturbations for a mode branch are solved for, the symbol $\tilde{x}_0$ corresponds to the spherical reference model. In all the following frequency steps for the same branch, $\tilde{x}_0$ represents the trial solution as obtained from extrapolation.

After applying a time window in the lag-time domain, we can represent the digitized function $g(\tau, \tilde{x}^n)$ as a finite-dimensional vector $\gamma(\tilde{x}^n)$. Suppressing the superscript for the branch number, n, we define the *a priori* probability density function (pdf) for the 'model' as follows:

$$\phi_{\text{prior}}(\tilde{x}) \propto \exp\left(-\frac{1}{2}((\tilde{x} - \tilde{x}_0)^T C_m^{-1}(\tilde{x} - \tilde{x}_0) + \lambda \tilde{x}^T H \tilde{x})\right), \tag{17}$$

where C_m stands for the *a priori* covariance matrix for the model $\tilde{x}$ (see Section 4.3). The factor $\lambda \tilde{x}^T H \tilde{x}$ (Section 4.4) represents a non-dimensional smoothness constraint, which stabilizes the retrieval process in the presence of nodes in the frequency spectrum (Trampert & Woodhouse 1995). The *a priori* distribution for the theory ϕ_{obs} and the data is given by

$$\phi_{\text{obs}}(\tilde{x}) \propto \exp\left(-\frac{1}{2}\gamma^T(\tilde{x})C_d^{-1}\gamma(\tilde{x})\right), \tag{18}$$

where C_d represents the covariance matrix of the data. Combining eqs (17) and (18) we can define the *a posteriori* pdf:

$$\phi_{\text{apost}} = \exp\left(-\frac{1}{2}\Phi(\tilde{x})\right), \tag{19}$$

where

$$\Phi(\tilde{x}) = \gamma^T(\tilde{x})C_d^{-1}\gamma(\tilde{x}) + (\tilde{x} - \tilde{x}_0)^T C_m^{-1}(\tilde{x} - \tilde{x}_0) + \lambda \tilde{x}^T H \tilde{x}. \tag{20}$$

The solution to the inverse problem is given by the maximum of ϕ_{apost}, which is equivalent to a minimum of $\Phi(x)$. We minimize $\Phi(\tilde{x})$ using an iterative scheme:

$$\tilde{x}_{k+1} = \tilde{x}_k + (G^T C_d^{-1} G + C_m^{-1} + \lambda H)^{-1}(G^T C_d^{-1}(d - \gamma(\tilde{x}))$$
$$- C_m^{-1}(\tilde{x}_k - \tilde{x}_0) - \lambda H \tilde{x}_k), \tag{21}$$

where G is the matrix containing the partial derivatives of γ with respect to $\tilde{x}$. This scheme is iterated until convergence is achieved. Note that we require the total perturbation with respect to the spherical reference model, $\tilde{x}$, to be smooth, and not the adjustment within each frequency window, $\tilde{x}_k - \tilde{x}_0$.

We approximate the *a posteriori* covariance matrix C_p by

$$C_p^{-1} = G^T C_d^{-1} G + C_m^{-1}, \tag{22}$$

which will be used to stabilize the retrieval of phase perturbations at extrapolated frequencies, as will be demonstrated in the next section.

4.3 *A priori* information

The inverse problem to retrieve phase perturbations from a seismogram, as described above, is strongly non-linear. However, the non-linear optimization scheme eq. (21) is stabilized by adding *a priori* information. Unfortunately, little is known about the size and character of overtone phase-velocity perturbations on a global scale, and to avoid biasing results, *a priori* information has to be included in a careful way. In eq. (21), *a priori* information is added through the *a priori* covariance matrix, C_m. This matrix should ideally represent the distribution of average phase velocities, for a given mode branch, that would be obtained when sampling the Earth along random paths. We choose to use the notion of how anomalous structure is mapped into phase velocities to estimate C_m.

We denote the spherical reference earth model with respect to a specific parametrization by a vector m^0. Using partial derivatives of the phase-velocity perturbations for mode branch n with respect to the model parameters, we can approximate to first order the eigenfrequency perturbation due to an average model perturbation along the path δm:

$$\delta\omega_l^n \approx \sum_j \frac{\partial\omega_l^n}{\partial m_j^0}\delta m_j = K_{lj}^n \delta m_j, \tag{23}$$

where j is an index over the model parametrization and l represents a specific angular order. Using this expression, we can approximate the distribution of phase-velocity perturbations given a distribution of model perturbations. We express the phase-velocity perturbation distribution in terms of $\tilde{x}^n$. Only evaluating at the nodes and assuming the linearity in eq. (23) holds, we write:

$$[\text{cov }\tilde{x}^n] = K^n[\text{cov }\delta m](K^n)^T, \tag{24}$$

where K^n represents the matrix containing the K_{lj}^n, as defined in eq. (23), at the nodal frequencies.

In order to carry out this calculation, we divide the mantle into some 110 layers with thicknesses of 25–40 km. We omit density and Q perturbations from δm in eq. (24) as it is likely that P- and S-velocity variations are the strongest influences on the phase-velocity perturbations of a mode branch. We assume the anomalous structure in each layer to be independent of that in other layers and the P and S perturbations to be uncorrelated. Furthermore, we assume that the global distribution of perturbations can be characterized by the same standard deviation, σ_m, at every depth level. For $[\text{cov }\delta m]$, only representing P- and S-velocity perturbations, we write:

$$[\text{cov }\delta m] = \delta_{ij}\sigma_m^2. \tag{25}$$

Combining eqs (24) and (25), and using kernels calculated from the spherical model, we can approximate $[\text{cov }x^n]$:

$$[\text{cov }\tilde{x}_n] \approx K^n I \sigma_m^2 (K^n)^T = \sigma_m^2 K^n(K^n)^T. \tag{26}$$

Thus defined, the off-diagonal elements of $[\text{cov }\tilde{x}^n]$ are determined solely by the similarity in sampling of heterogeneous structure at different frequencies within the same mode branch and not by assumed correlations between structure perturbations at different depth levels.

Definition (26) of the covariance matrix $[\text{cov }\tilde{x}^n]$ is used in the lowest-frequency window for which it is attempted to fit a certain mode branch. After having found the phase-velocity

perturbations in this window, the result is extrapolated to higher frequencies, as explained in Section 4.1. In this extrapolation step, the *a priori* information on the phase-velocity perturbations is better than that for the first frequency step, as one point along the smooth phase-velocity curve has already been found. This extra information needs to be quantified and included in the *a priori* covariance matrix.

After convergence of the iterative retrieval algorithm eq. (21), we use the linear approximation to the *a posteriori* covariance matrix eq. (22) to estimate the standard deviations for the retrieved phase perturbations. The standard deviations, as defined by the trace of C_p in eq. (22), are corrected for the estimated frequency-dependent number of free parameters in the lag-time window, giving standard deviations σ_i^n for the coefficients $\tilde{x}_i^n$. The standard deviation for the extrapolated phase velocity at $\bar{\omega}_{l+w+1}$ is estimated assuming that at the group arrival time, the phase at the extrapolated frequency is likely to be correct within $\epsilon\pi$, where ϵ is a specified small parameter (see below). Using group velocities as calculated from the reference earth model, this defines the *a priori* standard deviation σ_{l+w+1}^n for $\tilde{x}_{l+w+1}^n$:

$$\sigma_{l+w+1}^n = \frac{\epsilon\pi U^n(\bar{\omega}_{l+w+1})}{\Delta} ,\tag{27}$$

where $U^n(\omega)$ is the group velocity of branch n and Δ the epicentral distance. This estimate, combined with the corrected linear estimates from eq. (22), constitutes a complete set of *a priori* variances for the new frequency window.

To construct the *a priori* covariance matrix using the standard deviations defined above, we need to know how the perturbations at different frequencies are correlated. We define a correlation matrix V^n in terms of the covariance matrix $[\text{cov}\,\tilde{x}^n]$, eq. (26), for mode branch n as calculated from the spherical reference model:

$$V_{ij}^n = \frac{[\text{cov}\,\tilde{x}^n]_{ij}}{\sigma_i'\sigma_j'} ,\tag{28}$$

where

$$\sigma_i' = \sqrt{[\text{cov}\,\tilde{x}^n]_{ii}} .\tag{29}$$

Now, combining the estimated standard deviations with the correlation matrix V^n, the covariance matrix, after extrapolation for the window W_{l+1}, is given by:

$$C_{ij}^n = \sigma_i^n \sigma_j^n V_{ij}^n ,\tag{30}$$

where no contraction over i and j is understood and $i = l+1, l+w+1$ and $j = l+1, l+w+1$. This defines the *a priori* information on the phase-velocity perturbations used for the extrapolation steps in the iterative retrieval procedure.

The 'data' covariance matrix C_d in eqs. (18) and (21) is taken to be proportional to the identity matrix:

$$C_d = \beta\gamma_{\max}^2 I ,\tag{31}$$

where $\gamma_{\max}$ is the maximum element of the vector γ, β is an empirically determined real number and I is the identity matrix. The *a priori* data covariance thus defined is recalculated for every iteration in the iterative scheme given by eq. (21).

4.4 Parametrization and smoothness

An important aspect of any inverse problem is the parametrization. In this case, we seek to parametrize the phase

perturbations, as defined by the nodes $\bar{\omega}_i$, such that the expected variability within each branch is approximately evenly sampled. In this case, sampling is approximately even when the correlations between neighbouring nodes are similar at all frequencies. We define the parametrization by

$$\bar{T}_m = \frac{2\pi}{\bar{\omega}_m} = T_{\min} + (e^{\alpha(M-m)} - 1)\frac{T_{\max} - T_{\min}}{e^{\alpha(M-1)} - 1} ,\tag{32}$$

where $T_{\max}$ and $T_{\min}$ are the upper and lower limits of the parametrization in the frequency domain, expressed as periods, M is the number of nodes and α is a parameter that is adjusted to optimize the parametrization. The optimum α is determined by plotting and comparing the correlation matrices, as defined by eq. (28), for different values of α for several mode branches.

Imposing a smoothness constraint on the measured phase-velocity curves, as in eq. (17), implicitly imposes constraints on the variability with depth of earth models that are to be constructed using these measurements. We seek to minimize possible bias in such a model and define the smoothness to be non-dimensional with respect to the optimum parametrization. Assuming that the nodes in the frequency space are equidistant with respect to a new variable ψ, which is simply linear in the node numbering, the smoothness s of a phase-velocity perturbation curve $\delta\omega$ as a function of ψ is given by

$$s = \int_\Psi \left(\frac{\partial^2 \delta\omega(\psi)}{\partial\psi^2}\right)^2 d\psi .\tag{33}$$

Following Trampert & Woodhouse (1995), we write eq. (33) in terms of the model $\tilde{x}$:

$$\int_\Psi \left(\frac{\partial^2 \delta\omega(\psi)}{\partial\psi^2}\right)^2 d\psi = \int_\Psi \left(\sum_{i=1,m} \tilde{x}_i\left(\frac{d^2 D_i(\psi)}{d\psi^2}\right)\right)^2 d\psi = \tilde{x}^T H \tilde{x} ,\tag{34}$$

where

$$H_{ij} = \int_\Psi \frac{d^2 D_i(\psi)}{d\psi^2}\frac{d^2 D_j(\psi)}{d\psi^2} d\psi ,\tag{35}$$

which defines the factor $\lambda\tilde{x}^T H\tilde{x}$ in eq. (21).

4.5 Retrieving amplitude perturbations

Having retrieved the phase perturbations for branch n within a given frequency window, the algorithm attempts to fit the amplitudes as well. This is essential, as we seek to remove branch n from the data by fully fitting and then subtracting the synthetic mode-branch seismogram, as outlined in Section 3.

Combining eqs (5) and (7) we can write:

$$\tilde{u}_n(t,\tilde{x},\tilde{y}) = \sum_{i=1,M} \tilde{y}_i^n \sum_l D_i(\omega_l^n) A_l^n \exp\left[i(\omega_l^n + \delta\omega^n(\omega_l^n))t\right]$$

$$= \sum_{i=1,M} \tilde{y}_i^n \tilde{s}_i^n(t,\tilde{x}_n) ,\tag{36}$$

where $\tilde{s}_i^n(t)$, which we will call a *node seismogram*, is simply a waveform basis function with respect to the amplitude parametrization. We denote the estimate (from extrapolation in all windows, except for the lowest-frequency window) for $\tilde{y}_i^n$

before inversion for amplitudes by $\tilde{e}_i^n$ and define

$$\tilde{u}_n^0(t, \tilde{x}_n) = \sum_{i=1,M} \tilde{e}_i^n \tilde{s}_i^n(t, \tilde{x}_n). \tag{37}$$

The objective function we now seek to minimize for window $W_l(\omega)$ in terms of the amplitude adjustments $\tilde{y}_i^n$ is given by

$$k(\tau, \tilde{y}^n) = S'*\tilde{u}_n^0(t) - \left\{ \tilde{S}'^{-n}(t) + \sum_{i=l,l+w} \tilde{y}_i^n \tilde{s}_i^n(t) \right\}*\tilde{u}_n^0(t), \tag{38}$$

where the prime denotes a seismogram or a reduced seismogram, as in eq. (14). We use the algorithm eq. (21) to minimize eq. (38) as a function of $\tilde{y}^n$. In this case, eq. (21) does not have to be iterated, because eq. (38) is simply linear in $\tilde{y}^n$.

To stabilize the retrieval algorithm, *a priori* information needs to be added, as discussed above. However, very little is known about the size and character of overtone amplitude perturbations and no simple approximate relation between amplitude perturbations and heterogeneous structure can be used to estimate the distribution of amplitude perturbations. Therefore, we choose to add empirical *a priori* information which is very similar to that added for the retrieval of the phase: the smoothness constraint in eq. (21) is omitted ($\lambda = 0$) and we assume the amplitude perturbations of multiplets to be correlated in the same way as the phase perturbations. We define the initial *a priori* amplitude covariance by

$$C_m = \sigma_a^2 V^n, \tag{39}$$

where σ_a is chosen to optimally fit some trial data and V^n is the correlation matrix as defined by eq. (28). Extrapolation of the *a priori* covariance is identical to that followed for phase velocities (eqs 27–30), except for the definition of σ_{l+n+i}^n. Here we define

$$\sigma_{l+w+1}^n = \epsilon_a, \tag{40}$$

where ϵ_a is empirically chosen.

5 RELIABILITY OF MEASUREMENTS

An essential part of making measurements is assessing their reliability. In the case of waveform inversions, this is very difficult, in part because of the strong non-linearity of the inverse problem. In most surface-wave studies to date, measurements are either regarded as reliable and further used to constrain earth models, or deemed unreliable and discarded. When measuring properties of several mode branches independently from a single seismogram, there is the additional problem that after having completed the fitting procedure, we can only compare the waveform fit of the whole synthetic seismogram with the real data, as it is obviously impossible to determine the waveform fit of the individual mode-branch seismograms. Furthermore, the linear estimates from the *a posteriori* covariance matrix eq. (22) are useful in regularizing the inversion, but they are of limited use in establishing actual measurement errors.

Therefore, we have developed a method that helps to assess the reliability of the independent mode-branch measurements. The method is not theoretically rigorous, and absolute errors for the measurements cannot be determined. However, it defines a quantitative measure of reliability for each amplitude and phase measurement that can be used either to reject or to weight data.

First, we define the relative power, p^n, of a synthetic mode branch by

$$p^n = \exp -\sqrt{\frac{(\tilde{S}(t) - \tilde{u}_n(t))^2}{\tilde{u}_n^2(t)}}. \tag{41}$$

p^n is a measure of how much a synthetic mode-branch seismogram contributes to the total synthetic seismogram. It varies between 0 (no contribution) and 1 (only branch n contributes). We also define

$$\chi = \sqrt{\frac{(S(t) - \tilde{S}(t))^2}{\tilde{S}^2(t)}}, \tag{42}$$

which is simply a measure of how similar the full synthetic and the recorded waveforms are. Using χ, we define a new quantity f:

$$f = \frac{\mu^{(1-\chi)} - 1}{\mu - 1}, \tag{43}$$

where f varies between 0 (no fit) and 1 (perfect fit). In all examples shown in this paper, μ has been set to 11. This implies that a synthetic waveform that results in a variance reduction of 80 per cent is only about half as well 'fit', according to measure f, as a waveform that renders 100 per cent variance reduction.

The relative strength of a mode branch with respect to all other branches is strongly dependent on the group velocity and frequency windows considered. To account for this dependence, both p^n and f are bandpass filtered around the nodal frequencies $\bar{\omega}_i$ to give $p_{\bar{\omega}_i}^n$ and $f_{\bar{\omega}_i}$ and then calculated in N adjacent group-velocity windows. This defines two vectors, $p_{\bar{\omega}_i}^n$ and $f_{\bar{\omega}_i}$, where each element of the vectors corresponds to a specific group-velocity window. Using these two vectors, we define the reliability $r_{\bar{\omega}_i}^n$ of the amplitude and phase measurements of mode branch n at nodal frequency $\bar{\omega}_i$ by

$$r_{\bar{\omega}_i}^n = p_{\bar{\omega}_i}^n \cdot f_{\bar{\omega}_i}. \tag{44}$$

Doing this for all nodal frequencies, we can write:

$$r_{\bar{\omega}_i}^n = \sum_{j=1,M} P_{ji}^n F_{ji}, \tag{45}$$

where i is the index of the frequency nodes and j the time-interval index. P_{ij}^n is a matrix with the vectors $p_{\bar{\omega}_i}^n$ as rows and F_{ij} is a matrix with the vectors $f_{\bar{\omega}_i}$ as rows. Eq. (45) is visualized in Fig. 3 for the first overtone as retrieved in the example shown in Section 3.2. The reliability $r_{\bar{\omega}_i}^n$, as defined above, combines information about how much a synthetic mode branch actually contributes to the seismogram in the (ω, t) domain with how well the full data seismogram is fitted by a sum of all synthetic overtones in the same domain. This reliability estimate proves to be a very useful tool, as will be shown in the next section.

6 TESTS AND RESULTS

We have tested our algorithm extensively using a large number of synthetic and real data traces. In this section we present some representative results.

6.1 Synthetic tests

Synthetic tests are very useful to investigate to what extent phase and amplitude properties for several overtones can be
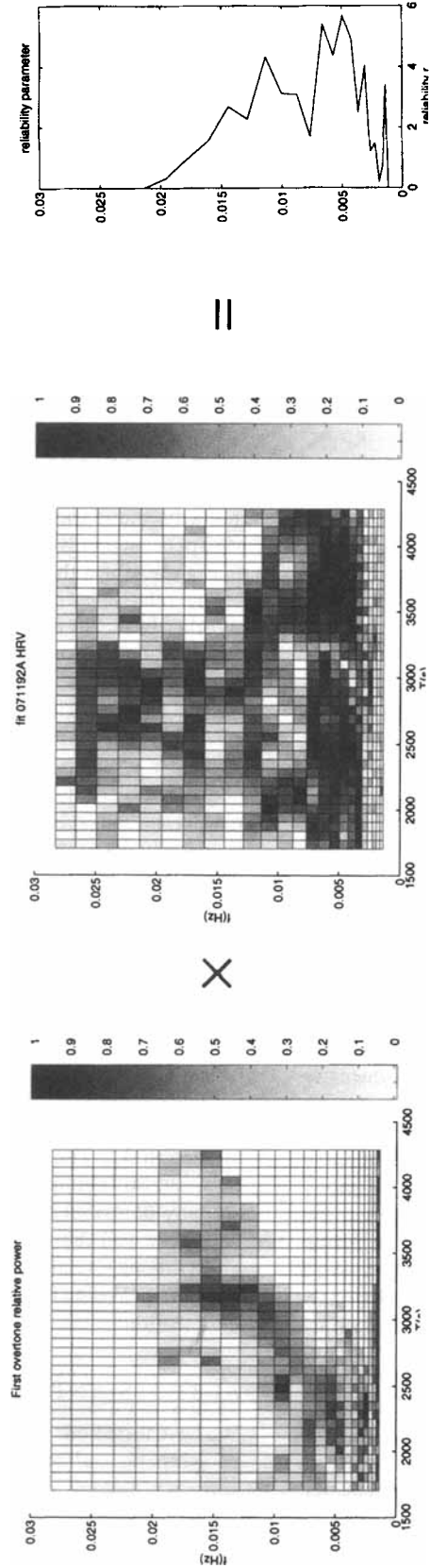
Figure 3. Graphic representation of how the reliability parameter $r_{\omega j}^n$ is determined, using the same seismogram as in Figs 1 and 2. The matrix on the left represents the relative power P_{ji}^1 of the first overtone as a function of time and frequency. The second matrix represents the waveform fit F_{ji} (see text for definitions of P_{ji}^1 and F_{ji}). The multiplication stands for the inner product between row i in the relative power matrix (i standing for a given frequency band) and row i in the waveform-fit matrix. This operation gives the result $r_{\omega j}^n$ (the reliability at frequency ω_j), which is plotted on the right. (It is interesting to compare the 'fit' matrix to the waveform fit in Fig. 1b.)

retrieved independently from a single seismogram. Although several assumptions, such as the absence of noise and the applicability of eq. (2), are made, synthetic tests give an indication of how the method will perform using real data. Furthermore, the tests shed light on the degree of uniqueness with which overtone properties can be retrieved.

In the example presented here, we use a synthetic vertical-component Rayleigh 'data' seismogram using input phase perturbations x_{inp}^n as calculated for the upper-mantle model M84C (Woodhouse & Dziewonski 1984). Random amplitude perturbations are also incorporated. The path and source used are the same as in the example in Section 3.1 and the 'data' seismogram is calculated using eq. (6) The synthetic seismogram thus constructed is used as input for the retrieval algorithm.

In this specific example, we consider only the eight lowest Rayleigh branches in the waveform fitting. The phase and amplitude perturbations are parametrized at 29 nodes between $T_{max} = 1000$ s and $T_{min} = 30$ s (eq. 32). The optimum parametrization parameter α in eq. (32) is set to 0.0017, $\sigma_m = 1$ per cent (eq. 25) and $\epsilon = 1/10$ (eq. 27). The smoothness parameter λ (eqs 17, 20, etc.) is set to 2×10^5. In Fig. 4(a) we show the waveform as predicted by PREM and the 'data' (both low-pass filtered, cut-off at $T = 40$ s). Clearly, there are significant phase and amplitude differences, especially in the arrivals just before the fundamental mode. However, after adjusting the phase and the amplitude of individual mode branches following the procedure outlined above, the agreement between synthetic and data is almost perfect, as shown in Fig. 4(b).

Having achieved agreement between the two waveforms, the question arises whether the underlying phase and amplitude perturbations have been retrieved correctly. In Fig. 5 we show the input and retrieved phase and amplitude perturbations for the fundamental mode, the second overtone and the fourth overtone, together with the corresponding reliability as a function of frequency as defined by eq. (45). The figure shows that, in specific frequency ranges, the phase and amplitude perturbations are retrieved correctly, whereas they are hardly retrieved in other ranges. The fact that phase and amplitude only have to be adjusted in specific frequency ranges to achieve good agreement between 'data' and synthetic demonstrates that mode branches only contribute significantly to the waveform in limited frequency bands. Importantly, the frequency bands of high reliability coincide with the frequencies for which the underlying perturbations are retrieved within acceptable errors, demonstrating the utility of the reliability estimates.

We have performed a great number of similar synthetic tests for both Rayleigh and Love waves with different smoothness requirements, different parametrizations, etc. In frequency bands where the reliability exceeds approximately 1 for overtones and 5 for the fundamental mode, perturbations are generally retrieved within small error bounds, largely independent of the *a priori* information used. This means that under specific assumptions, such as the existence of only fairly small and smooth (as a function of frequency) perturbations, probably only one set of phase and amplitude adjustments can be found in high-reliability frequency bands that explains the data. In that case, 'reliably' measured values seem likely to represent the true underlying perturbations.

6.2 Application to real data: *a priori* information

In this section, we demonstrate the stability of the retrieval process with respect to the added *a priori* information in an application to real data. We have applied the algorithm to the
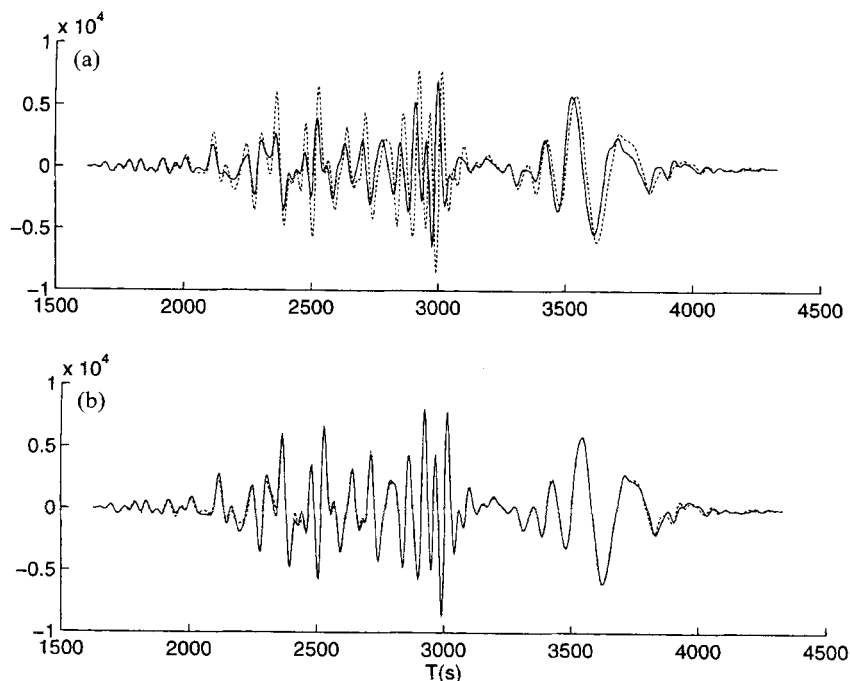

Figure 4. (a) Synthetic waveform 'data' that is used as input for our algorithm (dotted line). Source and path are the same as in the previous examples. Phase and amplitude perturbations are added as explained in the text. The solid line represents the starting waveform as calculated for the spherical reference model, PREM. (b) Final waveform fit obtained after adjusting the phase and amplitude of eight mode branches in specific frequency ranges.
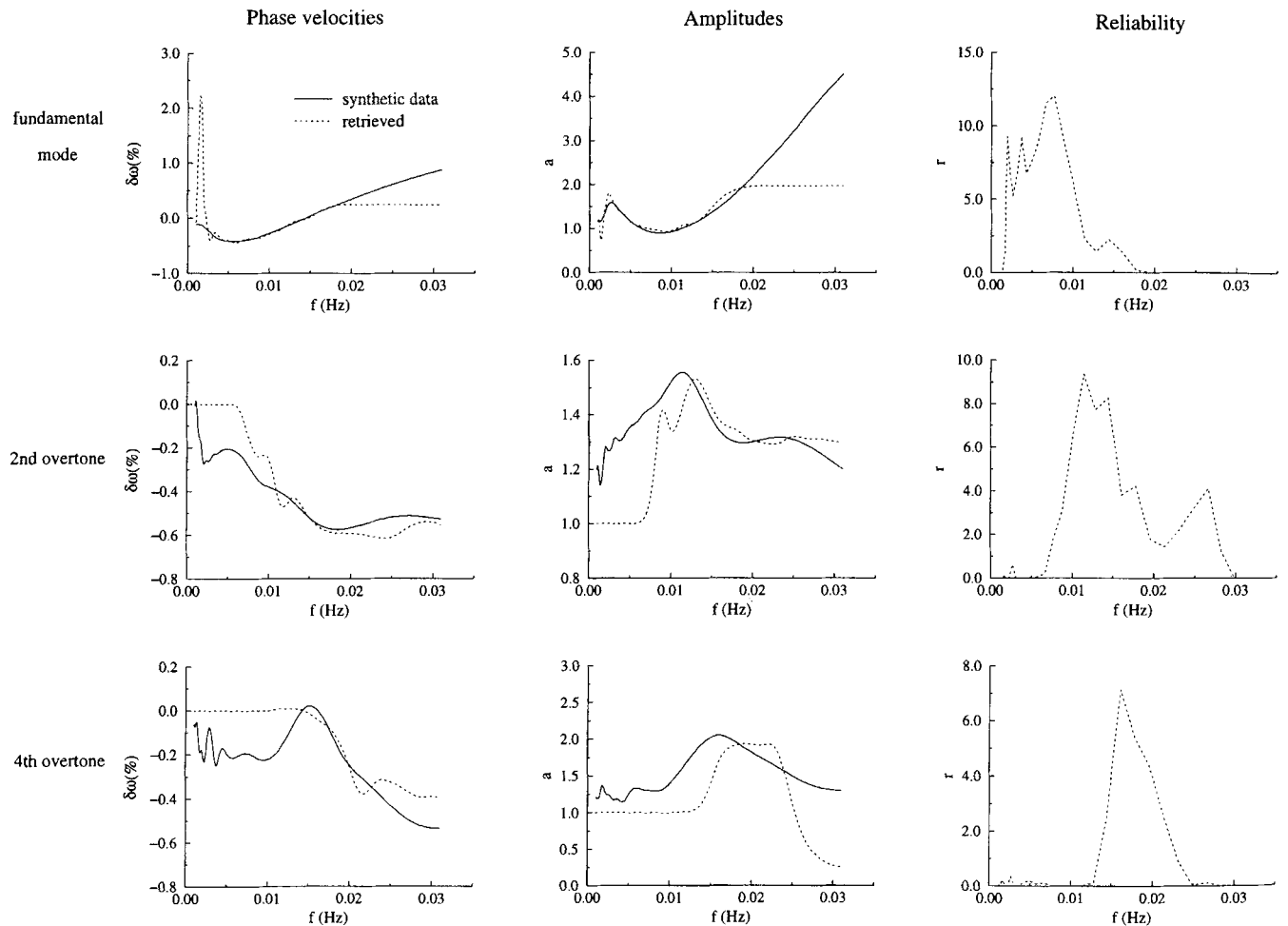
Figure 5. Input and retrieved phase-velocity and amplitude perturbations underlying the waveforms in Fig. 4(b). Results are shown for three mode branches (fundamental, second overtone, fourth overtone). The corresponding reliability is also shown. Note the good agreement between input and retrieved perturbations in frequency ranges where the reliability is high.

same real seismogram as in Section 3.1, using a great variety of settings for the parameters that determine the *a priori* information. Ideally, we want the measurements to be completely independent of the *a priori* information and therefore completely determined by the data. Of all the different types of *a priori* information applied, we present results for six representative cases, which are listed in Table 1.

After adjusting the phase and the amplitudes, the waveform fits for all but case 6 are good and comparable to the fit shown in

Table 1. Six combinations of parameters used in the algorithm as applied to the recorded waveform of Fig. 1. The numbers in brackets correspond to the equations where each parameter is introduced. The first overtone amplitude and phase-velocity perturbations retrieved for these cases are shown in Fig. 6.

run nr	σ_m (%) (25)	ϵ (27)	σ_a (39)	ϵ_a (40)	λ (17)	w (14)
1	1	.4	.1	.1	0	5
2	3	1.2	.1	.1	$2 \cdot 10^5$	5
3	1	.4	.1	.1	0	7
4	3	.8	.2	.2	$2 \cdot 10^5$	6
5	3	.8	.1	.1	$2 \cdot 10^5$	5
6	3	1.2	.1	.1	0	5

Fig. 1. In Fig. 6 the phase and amplitude measurements and the corresponding reliability estimate are shown for all six cases for the first overtone. At frequencies lower than 0.005 Hz, the phase and amplitude measurements are clearly not well constrained and are very sensitive to the regularization imposed, which is due to the fact that the signal-to-noise ratio is low at these long periods. In the frequency range 0.005–0.017 Hz, both the phase and the amplitude perturbations are much better constrained and largely independent of the *a priori* information added. As in the synthetic case, this range coincides very well with higher values of the reliability parameter. Note, however, that the phase measurement for case 6 deviates significantly from the other measurements for frequencies higher than 0.012 Hz. This deviation is not warranted by the data as the waveform fit for case 6 is worse than that for the other five cases, which is well reflected in the lower reliability for case 6. For all cases, at frequencies higher than 0.017 Hz the contribution of the first overtone to the waveform is small and the phase and the amplitude of the first overtone become poorly constrained, which is also clearly shown by the reliability parameter. Similar observations can be made about the relation between the amplitude measurements and the reliability estimate.

In this experiment and many others for both toroidals and spheroidals, the retrieved perturbations are largely
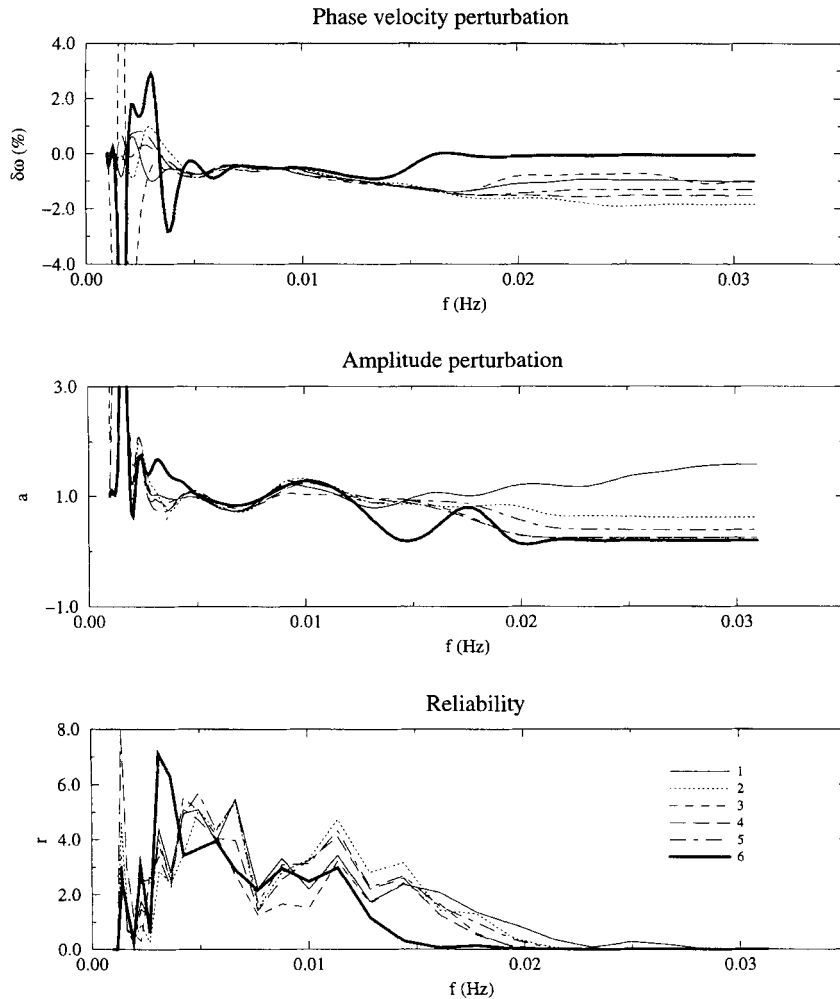
Phase velocity perturbation

Amplitude perturbation

Reliability

Figure 6. Phase-velocity and amplitude perturbations and reliability for the first overtone as determined for the six cases listed in Table 1 from the seismogram in Fig. 1. See text for details.

independent of the *a priori* information in high-reliability frequency ranges. This shows that the measurements are constrained by the data and not by *a priori* information.

6.3 Application to real data: starting models

An important question that arises when using our overtone phase-velocity perturbation measurement technique is whether the retrieved absolute phase velocities are independent of the starting model that is used. To investigate whether this is the case, we apply our technique for a range of starting models to data (Fig. 7, 205 paths) recorded for four randomly chosen earthquakes (Table 2). To test the stability of the method with respect to the starting model, we use, apart from PREM, four

different 3-D starting models that are derived from a realistic global 3-D model, R3d (Woodhouse 1993). For each path, we use the eigenfrequencies that are perturbed according to the average structure in the 3-D starting model along that path as values for ω_k in eq. (2). To mimic the use of starting models ranging from very good to very bad, we use as starting models the 3-D model itself (+1 case), half the heterogeneity of the starting model (+1/2 case), PREM, minus half the heterogeneity of the 3-D model (−1/2 case) and minus one times the heterogeneity of the 3-D model (−1 case). These five different starting models are intended to cover the widest possible range of starting models. In each case the relative measurements are converted to absolute measurements by adding the model perturbation to the relative perturbation.

Table 2. Source parameters for the four sources used in Section 6.3.

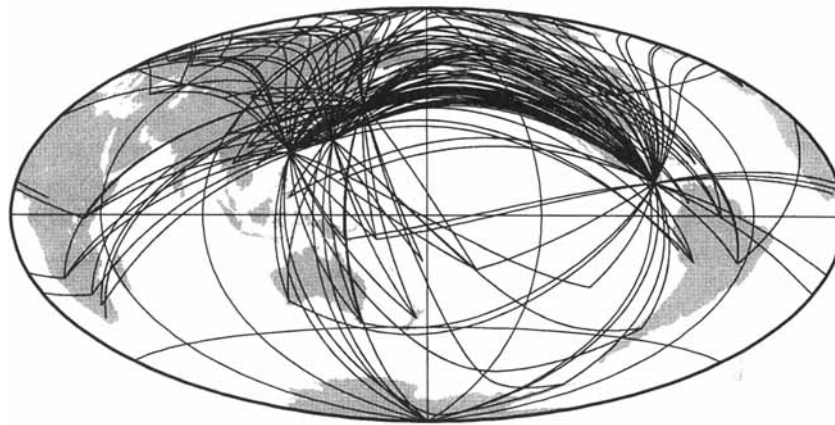| Harv. CMT cat.	longitude	latitude	depth (km)	M_0 (dyne-cm)	strike,dip,rake
030396D	-87.31	11.76	38.9	$1.27 \cdot 10^{26}$	95,120,63
030596B	122.08	23.94	24.0	$3.59 \cdot 10^{25}$	134,70,75
030996C	148.00	43.56	20.0	$1.55 \cdot 10^{25}$	112,33,77
031696C	139.12	29.12	477.9	$10.53 \cdot 10^{25}$	-163,322,84

Figure 7. The 205 great-circle paths used for the experiment with different starting models described in Section 6.3.

In Fig. 8 we compare the retrieved absolute phase velocities (expressed in terms of percentage perturbations relative to PREM) for three representative modes: the first overtone at 100 s; the second overtone at 56 s; and the fourth overtone at 47 s. Importantly, we plot only measurements with a reliability higher than 0.5 and for epicentral distances between 50° and 160°. In Fig. 8 all eigenfrequencies retrieved using the four starting models based on R3d are plotted on the *y*-axis against those retrieved using PREM as a starting model on the *x*-axis. Although some scatter can be observed, especially for the shorter-period high overtones, the same absolute phase velocities are retrieved to very good approximation, even for the worst case, the −1 starting model. The scatter falls well within reasonable observational errors (< ±0.5 per cent). The outliers that are observed are probably associated with 2π phase shifts.

To conclude, this experiment demonstrates the stability of the measurement process with respect to the starting model at moderately high reliabilities. As for the previous tests, this demonstrates that our measurements are constrained by data properties rather than anything else.

7 SIMILAR PATHS

As deviations from the spherical structure are relatively small in the Earth, one expects average phase-velocity perturbations to be similar for similar paths. Therefore, another way to test whether our algorithm is capable of retrieving the underlying phase-velocity perturbations is to apply it to a set of waveforms that have travelled along very similar paths.

In this example, we apply the algorithm to 90 vertical-component traces recorded in California. We have selected all 14 events with a moment larger than 10^{25} that occurred between 1990 and May 1995 in the region of Vanuatu and Santa Cruz islands. In Table 3 the Harvard CMT catalogue numbers and some relevant event parameters are listed. In Fig. 9 the corresponding great-circle paths are shown. We consider only vertical-component seismograms and we set $\sigma_m = 0.5$ per cent, $\epsilon = 1/4$ and $\lambda = 1 \times 10^6$ (compare with Section 6.1) and use PREM as the starting model. All traces are resampled at 4 s, detrended and have the mean removed. Source parameters are taken from the Harvard CMT catalogue. The parametrization of the phase and amplitude perturbations is the same as in all previous examples.

After application of the mode-branch stripping technique, the synthetics match the recorded waveforms very well. In Fig. 10 waveform fits are shown for three representative events: 052792A (large and shallow); 091592I (small and deep); and 032595C (small and intermediate). Waveform fits are excellent for all but a few traces. The traces that are not explained well are clearly noisy. In comparison to the clean traces, the noisy traces show anomalous amplitudes and waveforms. As there

Table 3. Source parameters for the 14 sources used in Section 7.

Harv. CMT cat.	longitude	latitude	depth (km)	M_0 (dyne-cm)	strike,dip,rake
092890B	166.84	-13.47	185.30	$1.20 \cdot 10^{26}$	173,53,83
081491D	167.83	-13.71	15.00	$6.63 \cdot 10^{25}$	2,74,151
101291B	166.36	-13.74	34.90	$2.30 \cdot 10^{25}$	161,55,94
040592C	166.14	-11.61	39.00	$1.73 \cdot 10^{25}$	167,62,85
052792A	165.06	-11.20	18.70	$3.90 \cdot 10^{26}$	340,56,-94
080492E	166.35	-11.73	97.30	$4.30 \cdot 10^{25}$	174,67,87
091592I	167.15	-14.02	195.90	$2.59 \cdot 10^{25}$	179,46,102
101592D	166.72	-14.44	51.50	$2.00 \cdot 10^{26}$	273,68,39
110492C	167.77	-14.17	15.00	$4.63 \cdot 10^{25}$	341,59,98
060393B	167.26	-14.71	143.60	$1.47 \cdot 10^{25}$	347,80,-115
072493D	167.05	-13.07	209.50	$1.17 \cdot 10^{25}$	332,54,64
042394B	167.72	-14.28	15.00	$1.66 \cdot 10^{25}$	336,58,96
082294F	166.46	-11.62	150.40	$1.99 \cdot 10^{25}$	356,47,98
032595C	165.91	-11.05	81.50	$2.05 \cdot 10^{25}$	180,57,61

First overtone: 100 s

Second overtone: 56 s

Fourth overtone: 47 s
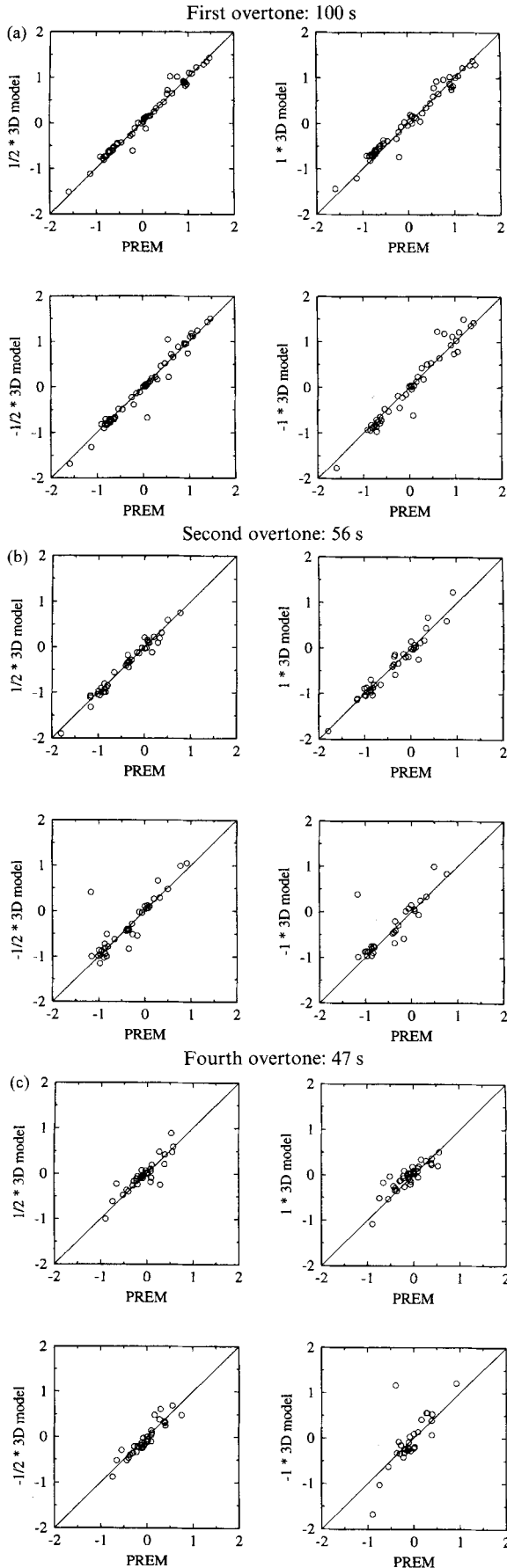
are many free parameters, it is essential that the inverse problem is constrained so that bad data cannot be fit; a good fit to bad data would almost certainly contribute erroneous phase and amplitude measurements.

Importantly, when we apply the *a priori* constraints mentioned above to waveforms for random globally distributed paths, we do not find considerably better fits for some regions than for others. Waveform fits for good data are usually excellent, whatever region of the Earth is sampled. This implies that the inverse problem is not overconstrained by unrealistic *a priori* information or hampered by assumptions inherent in the theory.

In Fig. 11 we present a scatter plot of reliability against retrieved phase velocity for the first Rayleigh-wave overtone at 100 s. Each circle represents a 'measurement' from one of the 90 seismograms. Not all of these circles represent actual measurements; most of the values that are clustered around the origin are from traces that the first overtone at this period was not inverted for because it did not meet the threshold mentioned under (7) in Section 3. In Fig. 11 the scatter in the phase-velocity perturbations decreases with increasing reliability, with the high-reliability measurements clustering around −0.7 per cent. As the measurements are independent, this distribution is highly significant, suggesting that we have indeed succeeded in measuring the underlying phase-velocity perturbations.

In Fig. 12(a) we show average phase-velocity perturbations for the fundamental-mode Rayleigh wave and the first four overtones as a function of frequency. The averages are calculated at the nodes of the parametrization from all measurements with a reliability higher than 0.5 for the overtones and higher than 5 for the fundamental mode. The number of measurements (out of a maximum of 90) that passes the reliability threshold and that is used to constrain the averages is also shown. The error bars, denoting one standard deviation, represent the scatter of the measurements at each node. The error bars show that well-constrained averages are obtained in a wide frequency range. Note that the phase-velocity perturbations for the overtones are smaller in size than those for the fundamental mode. This is not unexpected because the strongest heterogeneity in the Earth is found at shallow depths where the fundamental mode has a stronger sensitivity than the overtones.

In Fig. 12(b) similar averages are shown, but for reliabilities higher than 2 for overtones and higher than 10 for the fundamental mode. Although the averages in 12(b) are very similar to those in 12(a), the standard deviations are

Figure 8. (a) Comparison of absolute phase velocities (reliability higher than 0.5) retrieved for the first overtone at 100 s using PREM as a starting model (*x*-axis) with those retrieved using the four other starting models described in Section 6.3 (*y*-axis). The graphs correspond to (clockwise) the +1/2 R3d case, the +1 R3d case, the −1/2 R3d case and the −1 R3d case. The absolute phase velocities are given in per cent perturbation with respect to PREM. Each point corresponds to one specific seismogram. The line plotted on the graph is the line $x = y$. Clearly, the retrieved phase absolute phase velocities are largely independent of the starting model. (b) Same as (a) but for the second overtone at 56 s. (c) Same as (a) but for the fourth overtone at 47 s.
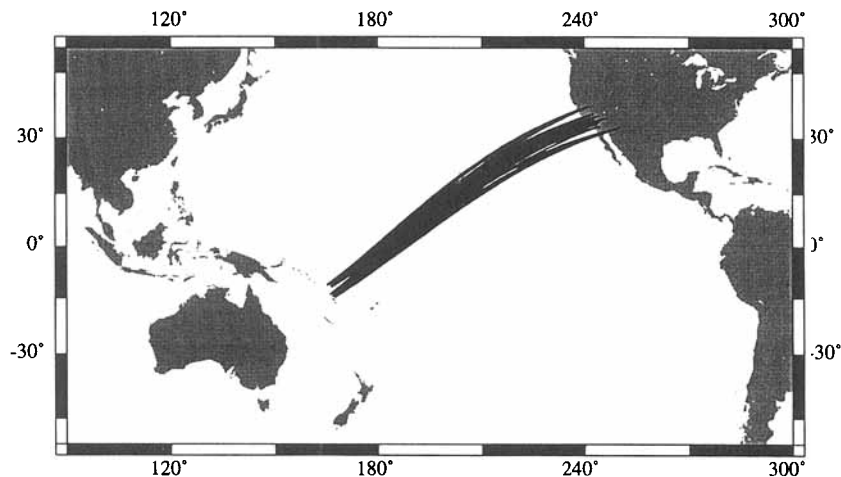
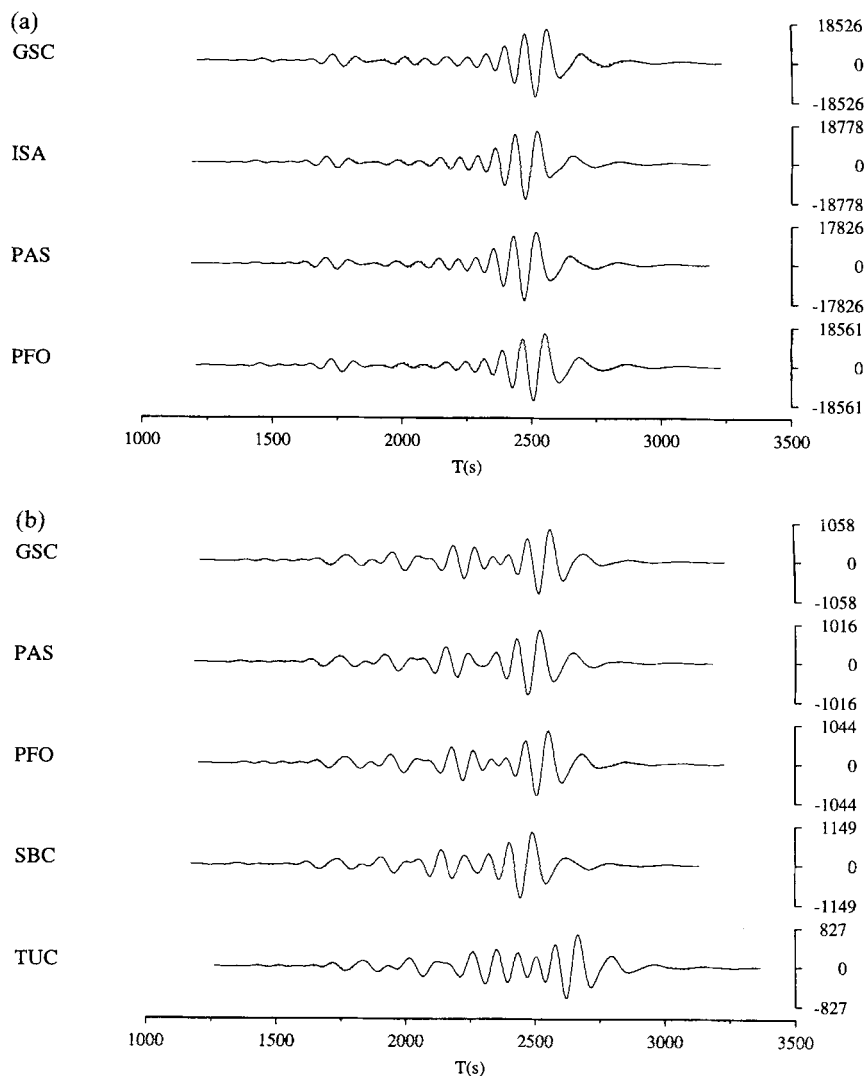**Figure 9.** Great-circle paths used in a similar paths experiment.

Figure 10. (a) Recorded (solid line) and synthetic (dotted line) waveforms for event 052792A. A group-velocity window (7.2–2.7 km s^{-1}) and a low-pass filter (cut-off at 60 s) are applied. Phase and amplitude have been adjusted for up to eight mode branches. Station names are shown on the left, the amplitude scale is shown on the right. (b) Same as (a) but for event 091592I. (c) Same as (a) but for event 032595C. For this event some waveforms cannot be fitted. The waveforms that are not well explained are clearly noisy: BAR—anomalous amplitudes and waveform; CALB—very large amplitudes at the beginning and end of the trace; DGR—anomalous amplitudes due to spike in signal; VTV—very small and noisy signal.

(c)

BAR

CALB

DGR

GSC

MLAC

NEE

PAS

PFO

TUC

VTV

```
7144
0
-7144

293
0
-293

18717
0
-18717

752
0
-752

105
0
-105

98
0
-98

758
0
-758

732
0
-732

543
0
-543

81
0
-81
```

1000   1500   2000   2500   3000   3500
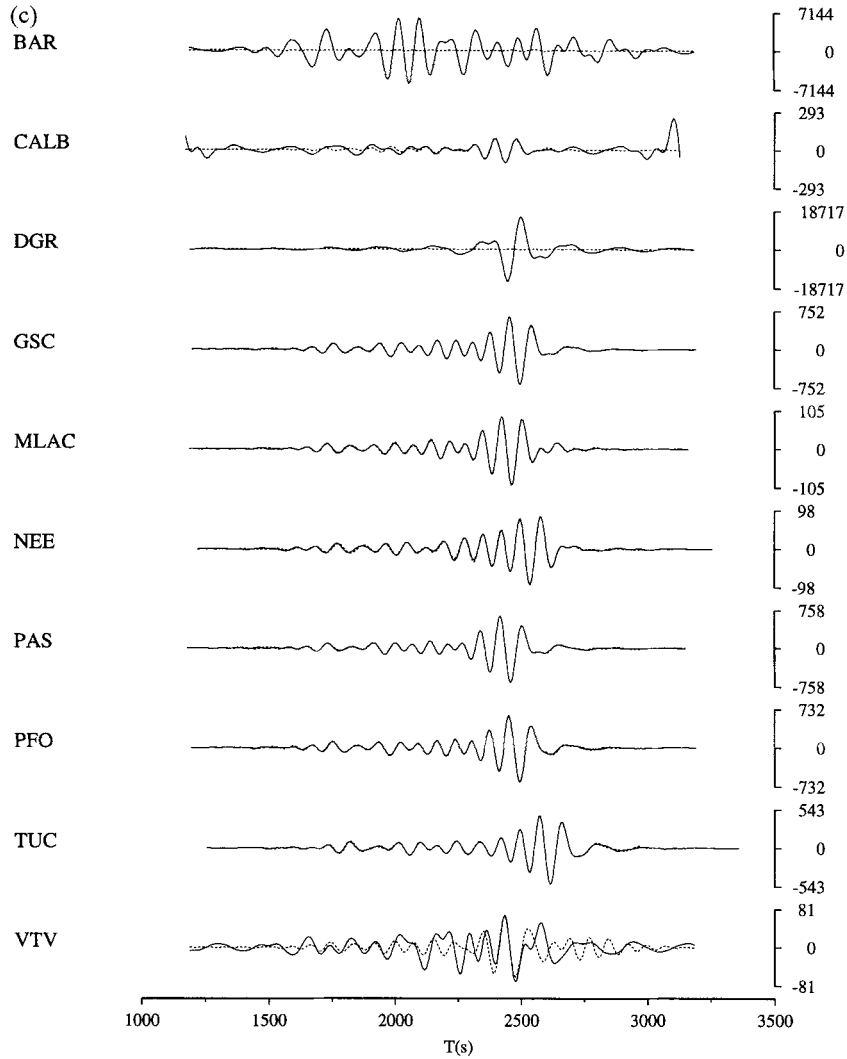
T(s)

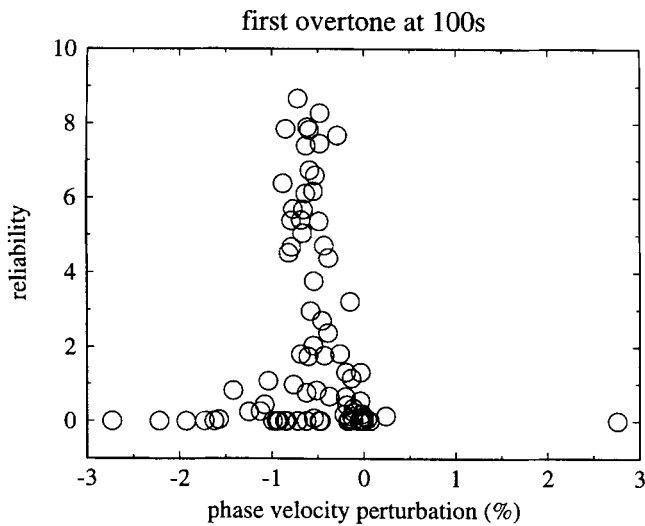**Figure 10.** (*Continued.*)

first overtone at 100s

Figure 11. Reliability plotted against phase-velocity perturbation for the first overtone at 100 s from all 90 traces. The higher reliability measurements cluster around −0.7 per cent, whereas the lower reliability measurements show a much larger scatter.

significantly smaller in (b). This again indicates a relation between the reliability parameter and the quality of the measurements.

Similar to the experiment in Section 6.2, we have applied the algorithm to the set of 90 waveforms using different *a priori* information. The average phase-velocity perturbations obtained of sufficiently reliable measurements are largely independent of the *a priori* information, confirming the validity of the approach.

The average amplitude perturbations that correspond to the phase data shown in Fig. 12(a) are shown in Fig. 13 with their respective standard deviations. Most striking are the positive amplitude perturbations for the second and third overtones at relatively short periods. It is very hard to interpret these anomalies because of the large number of factors that influence surface-wave amplitudes. Among the factors that could explain the amplitude measurements are anomalous mode branch excitations and a path-averaged Q structure different from that of PREM.

In Fig. 14 we compare our absolute phase-velocity measurements with those of Cara (1979) for the same path and phase velocities calculated for PREM. Both our and Cara's overtone phase velocities are slower than those of PREM,
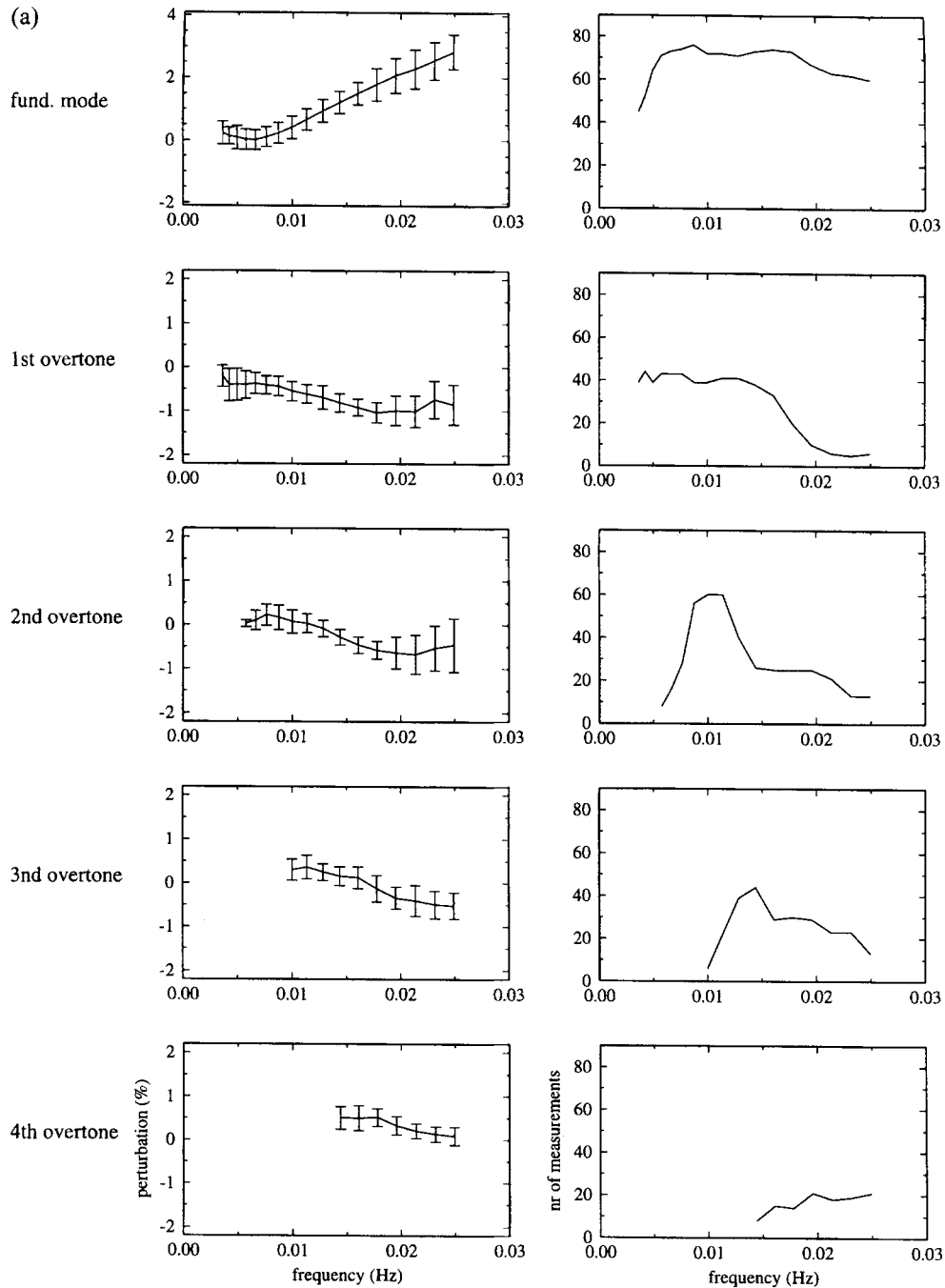
Figure 12. (a) Left column: average phase-velocity perturbations ($d \ln \omega$) as a function of frequency. Averages are calculated at the nodes of the parametrization. Only measurements with a reliability higher than 5 for the fundamental mode and 0.5 for the overtones are used to constrain the averages. The error bars show the standard deviation for each average. Right column: Number of measurements used to constrain each average as a function of frequency. (b) Same as (a) but for measurements with a reliability higher than 10 for the fundamental mode and higher than 2 for the overtones. The averages obtained are very similar to those in (a), but the averages are better constrained, despite the fact that the number of measurements used (right column) is considerably smaller. This is indicative of the relation between the reliability and the quality of a measurement.

but the size of the perturbations is quite different; our perturbations are about half the size of Cara's and outside the errors reported in his study. Interestingly, a similar discrepancy is observed for the fundamental mode. For comparison, we plot the path-averaged phase velocities calculated for the path between Vanuatu and California from the phase-velocity maps of Trampert & Woodhouse (1996). These predicted averages,

as well as the average phase velocities between 60 and 150 s calculated from the maps of Ekström, Tromp & Larson (1997) and those calculated from a regional study by Nishimura & Forsyth (1988) (both not plotted), agree very well with our measurements. The unexpected discrepancy, however, between our fundamental mode measurements and those of Cara suggests that a more detailed comparison of
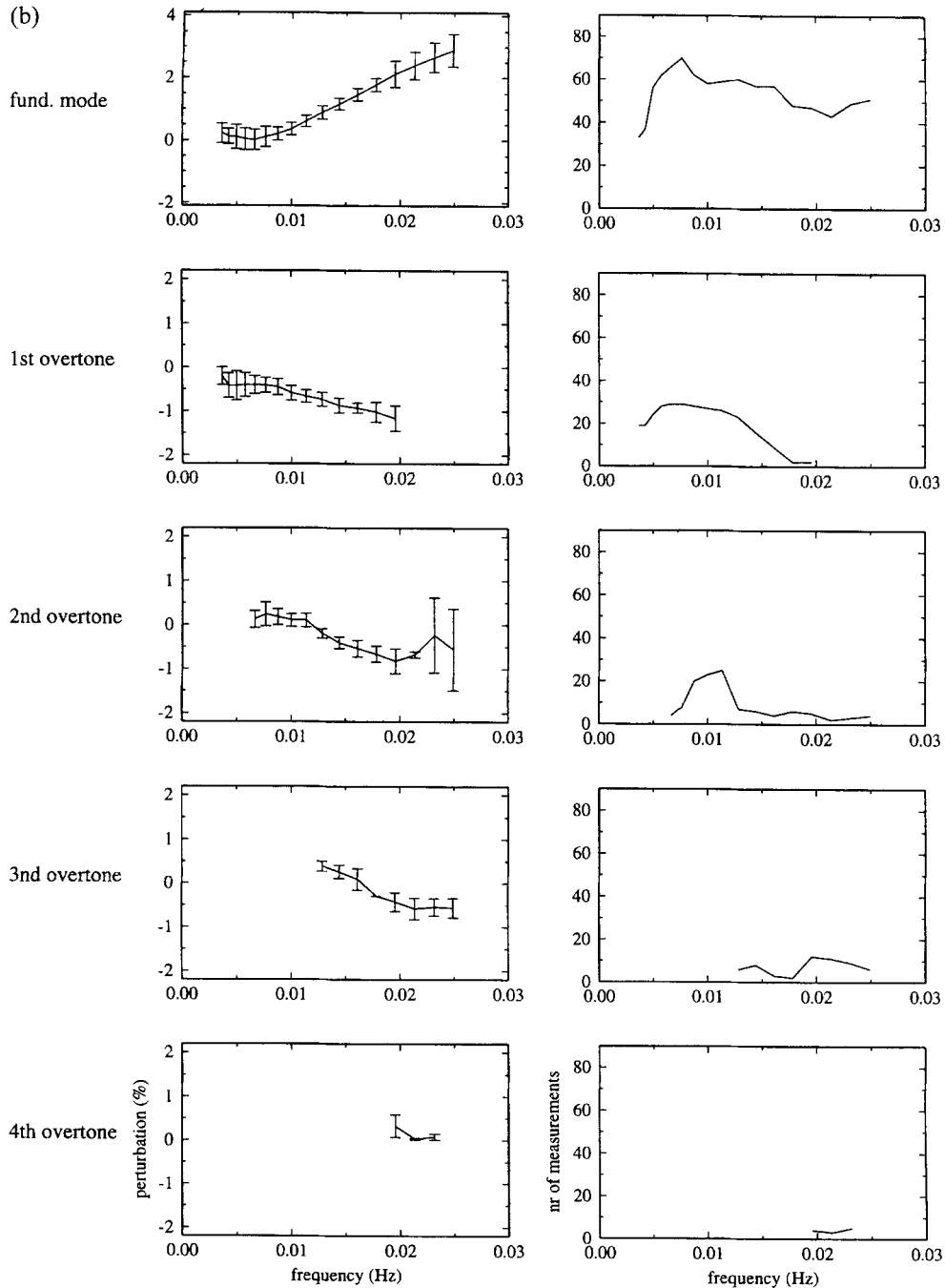
Figure 12. *(Continued.)*

the overtone phase-velocity measurements is probably not warranted.

As a final test of our measurements, we investigate to what extent the average phase velocities of all branches together can be explained by a simple path-averaged shear-velocity structure. We use the averaged phase-velocity perturbations weighted with respect to their respective variance reductions as data. Using a standard damped-least-squares technique, we invert these data for combined *P*- and *S*-wave velocity ($d \ln v_p = 0.5 d \ln v_s$). We parametrize the depth dependence of the model with 21 spline basis functions (Woodhouse & Trampert 1997). The resulting model (model A), expressed in

percentage perturbation with respect to PREM, is shown in Fig. 15. The variance reduction for the average phase-velocity perturbations is very high at 85 per cent. This indicates that the phase velocities of the different branches form a consistent set of measurements. Furthermore, the model exhibits exactly the features one would expect for a predominantly oceanic path: a fast oceanic lithosphere and a slow asthenosphere. To illustrate the effect of adding overtone phase velocities, we show a model constructed from only fundamental-mode phase velocities (model B, Fig. 15). The most striking difference between the two models is the extent of the low-velocity zone. This observation agrees very well with a previous study (Van
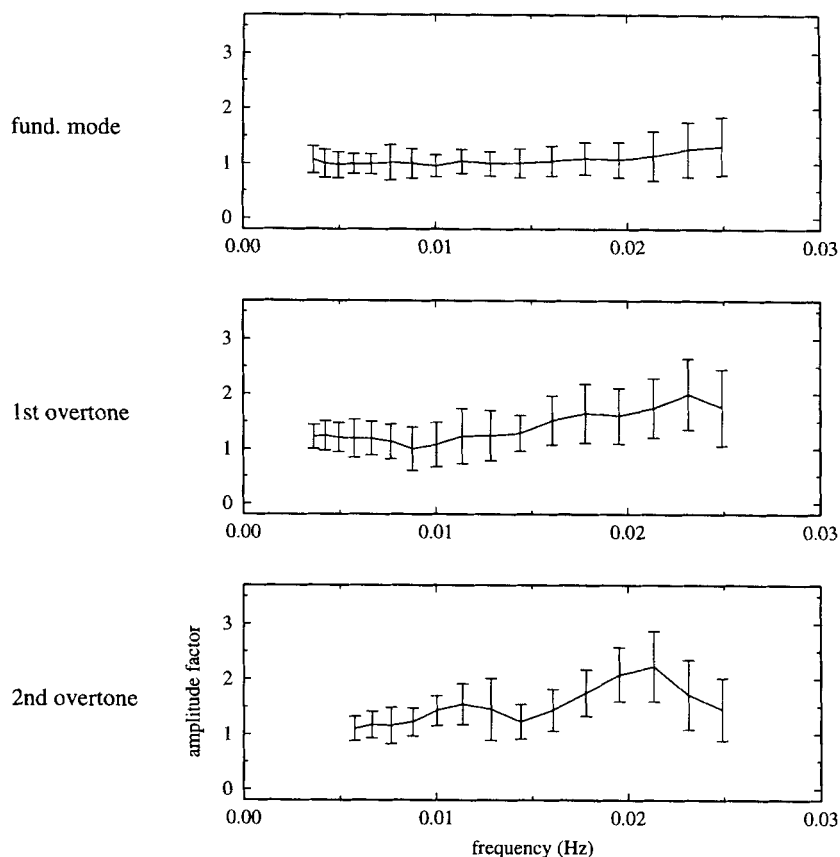
Figure 13. Average amplitude factors for the first three mode branches. The same reliability thresholds are used as in Fig. 12(a). The fundamental-mode amplitudes do not differ significantly from 1. Amplitudes for the first and second overtones, however, are significantly greater than 1 for frequencies higher than 0.015 Hz. Comparison with Fig. 12(a), right column, shows that the anomalous amplitudes occur at periods where the number of measurements constraining the averages decreases.

Heijst *et al.* 1994), which showed that a considerable degree of non-uniqueness exists when a velocity structure with a low-velocity zone is constrained by fundamental-mode phase velocities only. Therefore, unsurprisingly, model A explains the fundamental-mode data nearly as well as model B, whilst fitting the overtone data much better.

8 DISCUSSION

Using the new mode-branch stripping waveform-fitting technique presented in this paper, it is possible to find a set of phase-velocity and amplitude perturbations for several mode branches independently that explains both real and synthetic Rayleigh and Love waveforms well for periods down to approximately 35 s. Synthetic experiments show that in frequency bands where the reliability is high, the measured perturbations agree well with the values underlying the waveform. Moreover, synthetic tests and experiments with real data show that the technique is not very sensitive to the *a priori* information or the starting model used. In all the examples presented, the reliability parameter proves to be a very useful tool in assessing the quality of the measurements. Moreover, the experiments with real and synthetic data demonstrate that a high degree of uniqueness is achieved in frequency bands of high reliability *r*.

The experiment using 90 recorded waveforms that have travelled along very similar paths, demonstrates that overtone phase-velocity measurements agree well at high reliabilities. This encourages us to believe that true underlying phase-velocity perturbations are retrieved.

Finally, the new method has several advantages over methods that aim to retrieve path-averaged structures: branch-dependent off-great-circle propagation can be studied; measurements can be interpreted in terms of anisotropy; and the weighting of different mode branches as constraints on 3-D earth models can be done in a much more transparent way. Moreover, scaling of the waveform amplitudes is not required before inversion, allowing for mode-branch-dependent amplitude perturbations. These amplitude perturbations, apart from being essential for the mode subtraction, contribute further interesting data that can be interpreted in terms of attenuation and focusing.
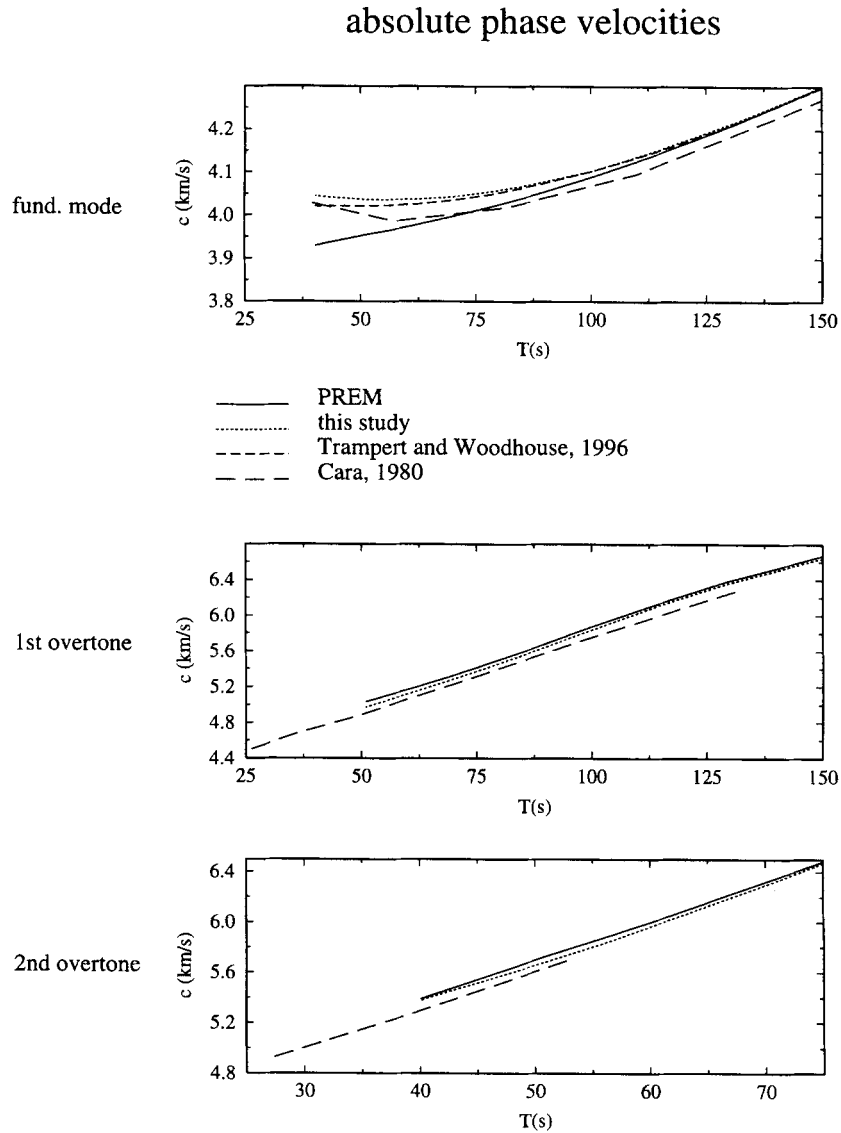
ACKNOWLEDGMENTS

absolute phase velocities

Figure 14. Absolute phase velocities for the Vanuatu–California path from PREM, from this study, from the phase-velocity maps of Trampert & Woodhouse (1996) and from the study by Cara (1979). See text for details.
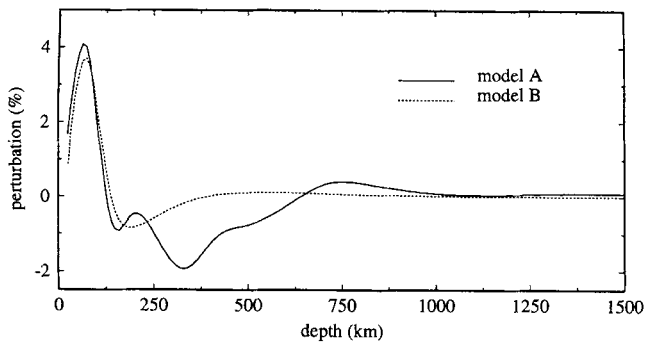

Figure 15. Average velocity perturbations with respect to PREM for the Vanuatu–California path. Model A is constrained using both fundamental and overtone phase velocities. Model B is constrained by fundamental-mode phase velocities alone. Model A shows stronger perturbations than model B below 300 km. These structures at greater depth can be resolved because overtone data is included.

REFERENCES

Cara, M., 1978. Regional variations of Rayleigh-mode velocities: a spatial filtering method, *Geophys. J. R. astr. Soc.*, **54**, 439–460.

Cara, M., 1979. Lateral variations of S-velocity in the upper mantle from higher Rayleigh modes, *Geophys. J. R. astr. Soc.*, **57**, 649–670.

Cara, M. & Leveque, J.J., 1987. Waveform fitting using secondary observables. inversion of multimode surface wave data, *Geophys. Res. Lett.*, **14**, 1046–1049.

Der, Z., Masse, R. & Landisman, M., 1970. Effects of observational errors on the resolution of surface waves at intermediate distances, *J. geophys. Res.*, **75**, 3399–3409.

Dziewonski, A.M., 1984. Mapping the lower mantle: Determination of lateral heterogeneity in P velocity up to degree and order 6, *J. geophys. Res.*, **89**, 5929–5952.

Dziewonski, A.M. & Anderson, D.L., 1981. Preliminary Reference Earth Model, *Phys. Earth Planet. Int.*, **25**, 297–356.

Ekström, G., Tromp, J. & Larson, E.W.F., 1997. Measurements and global models of surface wave propagation, *J. geophys. Res.*, in press.

Giardini, D., Li, X. & Woodhouse, J.H., 1987. Three-dimensional structure of the Earth from splitting in free oscillation spectra, *Nature*, **325**, 405–411.

Jordan, T.H., Puster, P., Glatzmaier, G.A. & Tackley, P., 1993. Comparison between seismic earth structures and mantle flow models based on radial correlation functions, *Science*, **261**, 1427–1431.

Lerner-Lam, A.L. & Jordan, T.H., 1983. Earth structure from fundamental and higher-mode waveform analysis, *Geophys. J. R. astr. Soc.*, **75**, 759–797.

Lerner-Lam, A.L. & Jordan, T.H., 1987. How thick are the continents?, *J. geophys. Res.*, **92**, 14 008–14 026.

Li, X.-D. & Romanowicz, B., 1995. Comparison of global waveform inversion with and without considering cross-branch coupling, *Geophys. J. Int.*, **121**, 695–709.

Li, X.-D. & Tanimoto, T., 1993. Waveforms of long-period body waves in a slightly aspherical earth model, *Geophys. J. Int.*, **112**, 92–102.

Marquering, H. & Snieder, R., 1995. Surface-wave mode coupling for efficient forward modelling and inversion of body-wave phases, *Geophys. J. Int.*, **120**, 186–208.

Masters, G., Jordan, T.H., Silver, P.G. & Gilbert, F., 1982. Aspherical earth structure from fundamental spheroidal mode data, *Nature*, **298**, 609–613.

Mitchell, R.G., 1980. Array measurements of higher mode Rayleigh wave dispersion: an approach utilising source parameters, *Geophys. J. R. astr. Soc.*, **63**, 311–331.

Nishimura, C.E. & Forsyth, D.W., 1988. Rayleigh wave phase velocities in the Pacific with implications for azimuthal anisotropy and lateral heterogeneities, *Geophys. J. Int.*, **94**, 479–501.

Nolet, G., 1975. Higher Rayleigh modes in Western Europe, *Geophys. Res. Lett.*, **2**, 60–62.

Nolet, G., 1977. The upper mantle under Western Europe inferred from the dispersion of Rayleigh modes, *J. Geophys.*, **43**, 265–285.

Nonweiler, T.R.F., 1984. *Computational Mathematics: An Introduction to Numerical Approximation*, E. Horwood, Chichester/Halsted Press, New York, NY.

Okal, E., 1978. A physical classification of the earth's spheroidal modes, *J. Phys. Earth*, **26**, 75–103.

Okal, E. & Jo, B.G., 1987. Stacking investigations of the dispersion of higher order mantle Rayleigh waves and normal modes, *Phys. Earth planet. Inter.*, **47**, 188–204.

Stutzmann, E. & Montagner, J.P., 1993. An inverse technique for retrieving higher mode phase velocity and mantle structure, *Geophys. J. Int.*, **113**, 669–683.

Stutzmann, E. & Montagner, J.P., 1994. Tomography of the transition zone from the inversion of higher mode surface waves, *Phys. Earth planet. Inter.*, **86**, 99–115.

Su, W.-J., Woodward, R.L. & Dziewonski, A.M., 1994. Degree 12 model of shear velocity heterogeneity in the mantle, *J. geophys. Res.*, **99**, 6945–6980.

Tanimoto, T., 1990. Long wavelength S-velocity structure throughout the mantle, *Geophys. J. Int.*, **100**, 327–336.

Tarantola, A. & Valette, B., 1982a. Inverse problems = quest for information, *J. Geophys.*, **50**, 159–170.

Tarantola, A. & Valette, B., 1982b. Generalized non-linear inverse problems solved using the least squares criterion, *Rev. Geophys. Space Phys.*, **20**, 219–232.

Trampert, J. & Woodhouse, J.H., 1995. Global phase velocity maps of Love and Rayleigh waves between 40 and 150 seconds, *Geophys. J. Int.*, **122**, 675–690.

Trampert, J. & Woodhouse, J.H., 1996. High resolution global phase velocity distributions, *Geophys. Res. Lett.*, **23**, 21–24.

Tromp, J. & Dahlen, F.A., 1992a. Variational principles for surface wave propagation on a laterally heterogeneous Earth—1. Time domain JWKB theory, *Geophys. J. Int.*, **109**, 581–598.

Tromp, J. & Dahlen, F.A., 1992b. Variational principles for surface wave propagation on a laterally heterogeneous Earth—2. Frequency domain JWKB theory, *Geophys. J. Int.*, **109**, 599–619.

Van Heijst, H.J., Snieder, R. & Nowack, R., 1994. Resolving a low-velocity zone with surface-wave data, *Geophys. J. Int.*, **118**, 333–343.

Wessel, P. & Smith, W.H.F., 1995. New Version of the Generic Mapping Tools Released, *EOS, Trans. Am. geophys. Un.*, **76**, 329.

Woodhouse, J.H., 1974. Surface waves in a laterally varying layered structure, *Geophys. J. R. astr. Soc.*, **37**, 461–490.

Woodhouse, J.H., 1983. The joint inversion of seismic waveforms for lateral variations in Earth structure and earthquake source parameters, *Proc. 'Enrico Fermi' Int. Sch. Phys.*, **LXXXV**, eds Kanamori, H. & Boschi, E., 366–397.

Woodhouse, J.H., 1993. Mantle models based upon GDSN and Geoscope waveform data and ISC arrival times, *IASPEI 27th General Assembly.*

Woodhouse, J.H. & Dziewonski, A.M., 1984. Mapping the upper mantle: 3-D modelling of Earth structure by inversion of seismic waveforms, *J. geophys. Res*, **89**, 5953–5986.

Woodhouse, J.H. & Dziewonski, A.M., 1986. 3-D mantle models based on mantle wave and long period body wave data, *EOS, Trans. Am. geophys. Un.*, **67**, 307.

Woodhouse, J.H. & Dziewonski, A.M., 1989. Seismic modelling of the Earth's large-scale 3-D structure, *Phil. Trans. R. Soc. Lond.*, A., **328**, 291–308.

Woodhouse, J. H. & Trampert, J., 1997. New geodynamical constraints from seismic tomography, *Earth planet. Sci. Lett.*, submitted.

Zhang, Y.S. & Lay, T., 1996. Global surface wave phase velocity variations, *J. geophys. Res*, **101**, 8415–8436.